Trophoblast glycoprotein is required for efficient synaptic vesicle exocytosis from retinal rod bipolar cells.

Colin M Wakeham[1], Qing Shi[1], Gaoying Ren[1], Tammie L Haley[1], Robert M Duvoisin[1], Henrique von Gersdorff[2], Catherine W Morgans[1]

[1]Department of Chemical Physiology & Biochemistry, Oregon Health & Science University, Portland, OR 97239, USA

[2]Vollum Institute, Oregon Health & Science University, Portland, OR 97239, USA

Corresponding Author

Catherine W Morgans
Chemical Physiology & Biochemistry, L-334
Oregon Health & Science University
3181 SW Sam Jackson Park Rd
Portland, OR 97239
Email: morgansc@ohsu.edu

Acknowledgements

This work was supported by NIH grants to CWM (R01 EY029985 and P30 EY010572) and HvG (R01 EY014043 and DC012938). The authors would like to thank R Lane Brown, Marc A Meadows, and André A Dagostin for assistance with patch clamp electrophysiology and data analysis.

Author contributions

Study design: CMW, RD, HvG, CWM; Experimentation: CMW, HS, GR, TLH; Data analysis: CMW, RD, HvG, CWM; Figure and manuscript preparation: CMW, RD, HvG, CWM; Editing and review: CMW, RD, HvG, CWM

Conflict of interest statement

The authors declare no conflicts of interest.

Abstract

Rod bipolar cells (RBCs) faithfully transmit light-driven signals from rod photoreceptors in the outer retina to third order neurons in the inner retina. Recently, significant work has focused on the role of leucine-rich repeat (LRR) proteins in synaptic development and signal transduction at RBC synapses. We previously identified trophoblast glycoprotein (TPBG) as a novel transmembrane LRR protein localized to the dendrites and axon terminals of RBCs. We now examine the effects on RBC physiology and retinal processing of TPBG genetic deletion in mice using immunofluorescence and electrophysiological techniques. The scotopic electroretinogram showed a modest increase in the b-wave and a marked attenuation in oscillatory potentials in the TPBG knockout. No effect of TPBG deletion was observed on RBC morphology, the localization of RBC signal transduction proteins, TRPM1 currents, or RBC excitability. Because scotopic oscillatory potentials primarily reflect RBC-driven rhythmic activity of the inner retina, we investigated the contribution of TPBG to downstream transmission from RBCs to third-order neurons. Time-resolved capacitance measurements indicated that TPBG deletion reduces synaptic vesicle exocytosis and subsequent GABAergic reciprocal feedback without altering voltage-gated Ca^{2+} currents. Thus, TPBG is required for efficient neurotransmitter release from RBCs to downstream cells. Our results highlight a novel synaptic role for TPBG at RBC ribbon synapses and support further examination into the mechanisms by which TPBG regulates RBC physiology.

Graphical abstract

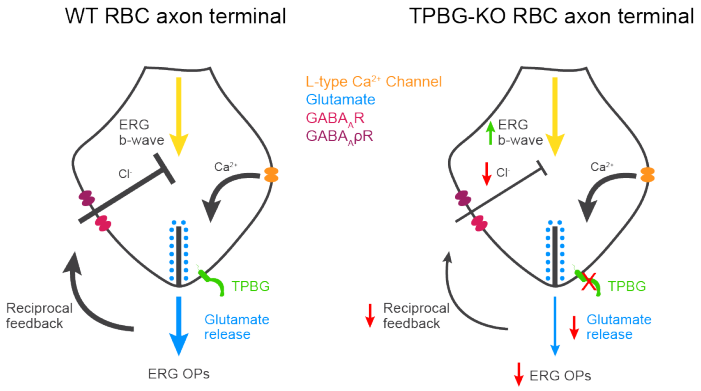

Introduction

Rod bipolar cells (RBCs) receive light-dependent synaptic input from rod photoreceptors in the outer plexiform layer (OPL) and drive retinal output by synapsing with AII amacrine cells (AII-ACs) in the inner plexiform layer (IPL). As the only dedicated bipolar cell in the primary rod

visual pathway, RBCs must be able to reliably transmit visual signals over the whole range of rod sensitivity. Accurate transmission of light signals requires precise synaptic targeting and tight control of signal transduction between RBCs and its synaptic partners. Identifying and characterizing the proteins required for the optimization and regulation of RBC synaptic development and function is essential for expanding our understanding of how RBCs contribute to vision.

Leucine-rich repeat (LRR) proteins form a large class of transmembrane proteins, each containing multiple leucine-rich motifs arranged to form extracellular protein binding domains (Kobe & Deisenhofer, 1994; Kobe & Kajava, 2001). Several LRR proteins identified in RBCs have been implicated in the development and maintenance of synaptic morphology and function. At synapses between photoreceptors and ON-bipolar cells, LRIT3 and nyctalopin are required for the localization of signal transduction components to the post-synaptic compartment (Cao, Posokhova, & Martemyanov, 2011; Hasan et al., 2019, 2020; Neuillé et al., 2017, 2015; Pearring et al., 2011). In RBC dendrites, LRRTM4 forms a trans-synaptic complex with rod spherules (Agosto & Wensel, 2020), whereas in RBC axon terminals, LRRMT4 is required for functional GABA receptor clustering, reciprocal feedback inhibition, and dyad synapse formation (Sinha et al., 2020). The ELFN family of LRR proteins form trans-synaptic complexes between photoreceptors and bipolar cells without which functioning connections fail to develop and retinal circuitry is mis-wired (Cao et al., 2015, 2020).

We recently identified trophoblast glycoprotein (TPBG, also called 5T4 or WAIF1 (Wnt-activated inhibitory factor 1)) in a phosphoproteomics screen as a novel LRR transmembrane glycoprotein in mouse RBCs that undergoes PKCα-dependent phosphorylation (Wakeham et al., 2019). TPBG contains eight N-terminal extracellular LRR motifs and a short intracellular C-terminal tail with a PDZ-interacting domain (Zhao, Malinauskas, Harlos, & Jones, 2014). TPBG localizes to the dendrites and synaptic terminals of RBCs and its expression is closely linked to eye opening and TRPM1 expression, suggesting that TPBG may play a role in RBC development or physiology (Wakeham, Ren, & Morgans, 2020).

Because the role of TPBG in the retina has not been established, we sought to characterize the effects of genetic knockout of TPBG in mouse RBCs using immunofluorescence confocal microscopy and electrophysiological techniques. RBC synapses form specialized active zones, each containing a synaptic ribbon, that permit a greater bandwidth of information transfer than conventional synapses. Ribbon synapses are noted for tight vesicle-Ca^{2+} coupling and a large supply of readily-available synaptic vesicles tethered close to the active zone (Dieck & Brandstätter, 2006; Morgans, 2000; Moser, Grabner, & Schmitz, 2020). In this study, we report

that TPBG is required for efficient synaptic vesicle exocytosis and neurotransmitter release at RBC ribbon synapses, implicating TPBG in ribbon synapse development and/or function.

Methods

Animals and statistical analysis

Constitutive TPBG knockout (TPBG-KO; KO) mice were B6;129S5-Tpbg^{tm1Lex}/Mmucd (MMRRC; UC Davis; Davis, CA, USA; Cat# 031630-UCD; RRID: MMRRC_031630-UCD). KO mice were purchased as cryopreserved sperm and reconstituted into a C57BL/6J (The Jackson Laboratory; Bar Harbor, M; Cat# 000664; RRID: IMSR_JAX:000664) background. Age-matched homozygous wild type (WT) littermates were used as controls. We used mice of both sexes and all mice were maintained on a 12-hour light/dark cycle and provided food and water ad libitum. Animals for immunofluorescence and electroretinogram experiments were 3-6 months old while animals used for patch clamp electrophysiology experiments were three months old. At least three mice were used from each condition for each experiment. All animal procedures were in accordance with the National Institutes of Health guidelines and approved by the Oregon Health & Science University Institutional Animal Care and Use Committee.

Statistical analyses were performed in Prism 9 (GraphPad; San Diego, CA, USA) and reported as mean ± SEM. We detected significance between conditions using unpaired Welch's *t*-tests and Brown-Forsythe ANOVA tests. Statistical significance is noted by asterisks (not significant (ns): $p > 0.05$; *: $p < 0.05$; **: $p < 0.01$; ***: $p < 0.001$; ****: $p < 0.0001$).

Immunofluorescence

Fresh eyecups were prepared from dissected eyes by cutting behind the ora serrata and removing the cornea and lens. For sectioning, eyecups were fixed for 30 min by immersion in fresh 4% paraformaldehyde (PFA) in PBS. The fixed eyecups were washed in PBS and then cryoprotected via sequential immersion in 10, 20, and 30% sucrose in PBS. Sections were cut at 20 μm thickness. Retina sections were post-fixed for 10 minutes in 4% PFA, blocked and permeabilized by incubation at room temperature for one hour in antibody incubation solution (AIS; 3% normal horse serum, 0.5% Triton X-100, 0.025% NaN_3 in PBS), and then incubated in primary antibodies diluted in AIS for one hour at room temperature. After washing with PBS, the sections were incubated in secondary antibodies diluted in AIS for one hour at room temperature. The slides were washed again in PBS and then mounted with VECTASHIELD PLUS antifade mounting media with DAPI (Vector Laboratories; Cat# H-2000-10).

128 For whole mount immunofluorescence, eyecups were fixed for 45 min by immersion in
129 fresh 4% PFA in PBS. The fixed eyecups were washed in PBS then retinas were removed prior
130 to blocking and permeabilization for one hour in AIS. The retinas were incubated in primary
131 antibodies diluted in AIS for four days at 4° C then washed overnight in PBST (PBS + 0.05%
132 Triton X-100) at 4° C. Retinas were incubated in secondary antibodies diluted in AIS overnight at
133 4° C then washed again in PBST. Finally, the retinas were mounted with VECTASHIELD PLUS
134 antifade mounting media.
135 Immunofluorescence images were taken with a Leica TCS SP8 X confocal microscope
136 (Leica Biosystems; Wetzlar, Germany) using a Leica HC PL APO CS2 63x/1.40 oil immersion
137 objective (Leica; Cat# 15506350). Brightness and contrast were adjusted equally across
138 genotypes using Fiji (Schindelin et al., 2012). A Gaussian blur using a radius of 0.5 pixels was
139 used to remove graininess from images. For image analysis of RBC axon terminals, a PKCα
140 binary was created in Fiji using default auto-thresholds to isolate RBC axon terminals. This binary
141 was then merged with the other channels to isolate PKCα-positive fluorescence. See figure
142 legends for specific information on Z-step distance and number of steps.
143
144 *Immunoblotting*
145 Retinas were extracted from freshly dissected eyes, suspended in chilled lysis buffer (50
146 mM Tris pH 7.4, 150 mM NaCl, 1 mM EDTA, 1% Triton X-100, 1% deoxycholate, 0.1% SDS) with
147 1X protease/phosphatase inhibitor cocktail (Cell Signaling Technology; Danvers, MA, USA; Cat#
148 5872) and homogenized with a Teflon-glass homogenizer. The lysate was centrifuged for 15
149 minutes at 16,400 rpm and 4° C, and the pellet was discarded. Retinal lysates were diluted to a
150 protein concentration of 1 μg/μl in lysis buffer and brought to 1X NuPAGE LDS Sample Buffer
151 (Thermo Fisher Scientific; Cat# NP0007) and 1X NuPAGE Sample Reducing Agent (Thermo
152 Fisher Scientific; Cat# NP0009). Pre-cast NuPAGE 1 mm 4-12% Bis-Tris gels (Thermo Fisher
153 Scientific; Cat# NP0322BOX) were loaded and run at 200 V and 140 mA for 55 minutes in 1X
154 NuPAGE BOLT SDS Running Buffer (Thermo Fisher Scientific; Cat# B0001).
155 Proteins were transferred onto PVDF membranes using a wet transfer system and 1X
156 NuPAGE Transfer Buffer (Thermo Fisher Scientific; Cat# NP00061) with 5% MeOH at 300 mA
157 for two hours. The membranes were then rinsed with methanol and blocked for one hour in
158 Odyssey Blocking Buffer TBS (LI-COR Biosciences; Cat# 927-50003) on a shaker at room
159 temperature, before being incubated in primary antibody diluted in Odyssey buffer at 4° C
160 overnight. The membranes were washed in TBST (Tris-buffered saline with 0.1% Tween-20),

161 then incubated in secondary antibody diluted in Odyssey buffer for one hour at room temperature
162 before being washed in TBST. Dried blots were imaged using a LI-COR Odyssey CLx Imaging
163 System at 680 and 800 nm.
164
165 *Electroretinogram recording*
166 Mice were dark-adapted overnight and prepared for recording under dim red light.
167 Anesthesia was initiated via IP injection of ketamine:xylazine (100:10 mg/kg) and maintained with
168 booster injections (30:3 mg/kg) at approximately 30 minute intervals until completion of the
169 experiment. Body temperature was maintained at 36.5-38° C. Before recording, the pupils were
170 dilated with 2.5% phenylephrine and 1% tropicamide, and the cornea was anesthetized with 1%
171 topical proparacaine. A wire loop placed under the upper teeth was used to draw the mouse into
172 a custom-made holder that stabilized the head and permitted delivery of 95% O_2/5% CO_2
173 (carbogen; ~0.25 l/min). The recording was made using a custom contact lens electrode featuring
174 a central platinum wire placed against the cornea with a small drop of hypromellose to prevent
175 drying. A loop electrode placed behind the eye served as a reference electrode and a needle
176 electrode placed in the tail served as a ground. The mice were placed in a Ganzfield sphere and
177 light stimuli were provided by custom 502 nm LED photostimulators. Light stimulus intensity was
178 controlled with neutral density filters and by altering flash duration and was measured post-hoc
179 with an ILT5000 radiometer (International Light; Newburyport, MA; USA) using a scotopic filter.
180 Traces were recorded with customized software (ERGLab; Richard Weleber; Casey Eye Institute;
181 Portland, OR, USA).
182 Full-field scotopic electroretinograms (ERGs) from both eyes were recorded
183 simultaneously after a series light flashes ranging from 8.71×10^{-1} to 8.51×10^{1} cd•s/m^2 (-0.06 to
184 1.93 log(cd•s/m^2) (Xiong et al., 2015). For dimmer intensities (-1 to 0 log(cd•s/m^2)), three trials
185 were averaged with inter-flash intervals of 20 seconds. For brighter intensities (0 to 2
186 log(cd•s/m^2)), two trials were averaged with inter-flash intervals of 30 to 120 seconds.
187 ERGLab data was exported for offline processing using a custom Python script and the
188 SciPy package (https://docs.scipy.org/doc). Statistical analyses were performed in Prism 9
189 (GraphPad; San Diego, CA, USA). The start of the flash stimulus was set to time zero and traces
190 were baselined. A-waves and b-waves were isolated using a low-pass filter (60 Hz) and OPs were
191 isolated with a Butterworth band-pass filter (30-300 Hz) and the "signal.filtfilt" function in SciPy
192 (**Figure 2: Supplementary Figure 1**). The a-wave amplitudes were measured from baseline-to-
193 trough, b-wave amplitudes were measured from a-wave trough-to-b-wave peak, and the b/a-wave
194 ratio was calculated to normalize responses. OP amplitude was measured from trough-to-peak

195 of the largest wave and the OP/b-wave ratio was calculated using b-wave amplitudes from the
196 same recording.
197
198 *Patch clamp electrophysiology*
199 Retinas were isolated and embedded in 3% low melting point agarose (Sigma; Cat#
200 A0701) in carbogenated bicarbonate-buffered Ames medium (Ames & Nesbett, 1981; Ames
201 Medium w/L-Glutamate; US Biological; Swampscott, MA, USA; Cat# A1372-25) and 200-250 μm
202 slices were prepared with a Leica VT1200 vibrating microtome. For chemically simulated light
203 response experiments, retinas were sliced in carbogenated Ames. For all other recordings, slicing
204 was performed in chilled and carbogenated low-Na^+, high-sucrose cutting solution containing (in
205 mM): 210 sucrose, 35 $NaHCO_3$, 20 HEPES, 10 glucose, 6 $MgCl_2$, 3 sodium pyruvate, 2.5 KCl and
206 0.5 $CaCl_2$ and buffered to pH 7.4 with NaOH. Retina slices were stored at room temperature in
207 carbogenated Ames medium before being transferred to the recording chamber. Heated (31-33°
208 C) Ames medium was continuously perfused over the retinal slices during all patch-clamp
209 recordings.
210 Thick-walled borosilicate glass pipettes (World Precision Instruments; Sarasota, Fl, USA;
211 Cat# 1B150F-4) were pulled using a Narishige PP-830 electrode puller (Tokyo, Japan). Ultrapure
212 salts were purchased from Sigma-Aldrich (St. Louis, MO, USA). For RBC visualization, the
213 fluorescent tracer Alexa Fluor 594 Hydrazide (100 μM; Thermo Fisher Scientific; Cat# A10438)
214 was added to the pipettes. Whole-cell voltage-clamp and current-clamp recordings were
215 performed in photopic conditions using a double EPC-10 patch clamp amplifier controlled by
216 Patchmaster software (HEKA Elektronik, Lambrecht/Pfalz, Germany) or an Axon Axopatch 200B
217 controlled by pCLAMP software (Molecular Devices; San Jose, CA, USA). Data was acquired at
218 a 20 kHz sampling rate and filtered with a 2.9 kHz low-pass Bessel filter. RBCs were targeted
219 visually using Dodt gradient contrast microscopy and confirmed post-hoc with cell-filling and
220 epifluorescence microscopy. Both pCLAMP and Patchmaster data sets were exported to Igor Pro
221 (WaveMetrics, Lake Oswego, OR, USA) for offline analysis with custom Igor scripts and statistical
222 analysis was performed in Prism. We used a P/10 leak subtraction protocol (-80 mV to -73 mV)
223 in voltage-clamp to isolate voltage-gated Ca^{2+} currents and GABAergic feedback currents; leak
224 traces for each trial were baselined, summated, and subtracted from the raw pulse trace.
225 To record chemically simulated light responses, pipettes were pulled to 10-12 MΩ and
226 backfilled with a potassium gluconate solution containing (in mM): 125 K-gluconate, 8 KCl, 5
227 HEPES, 1 $MgCl_2$, 1 $CaCl_2$, 3 adenosine 5'-triphosphate magnesium salt (Mg-ATP), 0.5 guanosine
228 5'-triphosphate disodium salt (Na_2-GTP), and 5 EGTA, and pH was adjusted to 7.3 with KOH. The

229 Ames medium was supplemented with 4 μM L-(+)-2-amino-4-phosphonobutyric acid (L-AP4), an
230 mGluR6 agonist, to maintain a simulated dark-adapted state. A puffer pipette (12-18 MΩ) was
231 maneuvered into the dendritic field of the target cell, and the cell was patched in voltage-clamp
232 and held at -60 mV. The mGluR6 antagonist [RS]-α-cyclopropyl-4-phophophenylglycine (CPPG)
233 was applied directly to the dendrites using a Picospritzer II (Parker Hannifin; Hollis, NH, USA; 600
234 μM at 20 psi) for five seconds and the RBC response was recorded. For each cell, four sweeps
235 were recorded at 15-second intervals.

236 For current-clamp experiments, pipettes were pulled to 9-12 MΩ and backfilled with a
237 potassium gluconate solution containing (in mM): 104 K-gluconate, 10 KCl, 10 HEPES, 4 Mg-
238 ATP, 0.4 Na_2-GTP, 10 Na_2-Phosphocreatine, and 2 EGTA, and pH was adjusted to 7.3 with KOH.
239 The Ames medium was supplemented with 1 mM $CaCl_2$ and the synaptic blockers (in μM): 0.5
240 strychnine (glycine receptor blocker), 3 gabazine (SR 95531; $GABA_A$ receptor blocker), 50
241 [1,2,5,6-tetrahydropyridin-4-yl]methylphosphinic acid (TPMPA; $GABA_A\rho$ receptor blocker), and 4
242 L-AP4 to block excitatory and inhibitory inputs. The total external $CaCl_2$ concentration was
243 estimated to be 2.15 mM. Cells were first patched in voltage-clamp and then the amplifier was
244 switched to fast current-clamp mode using the EPC-10 Gentle CC-Switch feature. Resting
245 membrane voltage was recorded at 0 pA and then current was injected for 100 ms from -80 pA
246 to 80 pA in 20 pA steps. Peak voltage was measured as the peak (min or max) voltage
247 immediately after the onset of the current pulse, and sustained voltage was measured as the
248 average over the final 10 ms of the pulse. For each cell, five sets of sweeps were recorded at
249 five-second intervals.

250 For the remaining experiments, the pipettes were pulled to 5-8 MΩ and backfilled with a
251 cesium gluconate solution containing (in mM): 94 Cs-gluconate, 10 HEPES, 20 tetraethyl
252 ammonium chloride (TEA-Cl), 4 Mg-ATP, 0.4 Na_2-GTP, 10 Na_2-Phosphocreatine, and 2 EGTA,
253 and pH was adjusted to 7.3 with CsOH.

254 For voltage-clamp time-resolved capacitance recordings, the Ames medium was
255 supplemented with 1 mM $CaCl_2$ and (in μM): 0.5 strychnine, 3 gabazine, 50 TPMPA, and 4 L-AP4
256 to isolate voltage-gated Ca^{2+} currents and maximize membrane resistance. Pipettes were
257 wrapped with parafilm to reduce pipette capacitance and electrical noise. Membrane capacitance
258 (C_m), membrane resistance (R_m), and series resistance (R_s) were measured using the "sine + DC"
259 method implemented in Patchmaster software (Balakrishnan, Puthussery, Kim, Taylor, &
260 von Gersdorff, 2015; Gillis, 2000; Oltedal & Hartveit, 2010). Exocytosis was evoked in voltage-
261 clamp mode with a 100 ms depolarizing pulse from -80 mV to -10 mV to activate voltage-gated

262 Ca^{2+} currents. Resting C_m was measured using a sinusoidal voltage command (200 Hz, 30 mV
263 trough-to-peak) superimposed over the membrane holding potential (-80 mV) and one
264 measurement was generated per cycle (**Figure 5A**). An increase in exocytosis (ΔC_m) was
265 measured from the change in C_m values before and after the depolarizing pulse. A baseline was
266 established by averaging the resting C_m over the one second immediately preceding the voltage
267 step. C_m measurements immediately after repolarization were excluded from analysis to allow for
268 the full decay of evoked conductances and C_m was averaged over the following 500 ms. Cells
269 were discarded if changes in C_m correlated significantly with changes in R_m or R_s. For each cell,
270 five sets of sweeps were recorded with 15 second intervals. To remove noise, C_m data was filtered
271 through a 5 Hz low-pass FIR filter. When different frequency sinusoidal voltage commands were
272 used (**Figure 5: Supplementary Figure 1**), recordings were resampled to 200 Hz for ease of
273 comparisons.
274 To record reciprocal inhibitory currents, the Ames medium was supplemented with 1 mM
275 $CaCl_2$, 4 μM L-AP4, and 0.5 μM strychnine. Feedback current was evoked in voltage-clamp mode
276 with a 100 ms depolarizing pulse from -80 mV to -10 mV to activate voltage-gated Ca^{2+} currents
277 and subsequent outward GABAergic inhibitory currents. Inhibitory current amplitudes were
278 measured from a baseline established at the peak inward current after depolarization, which was
279 very similar to peak Ca^{2+} currents (**Figure 7B)**. Sustained currents were averaged over the final
280 10 ms of the depolarizing pulse and charge transfer was measured as the area between the curve
281 and the baseline. Five sets of sweeps were recorded at five-second intervals.
282
283 **Results**
284 *TPBG is not required for normal gross RBC morphology*
285 We used the constitutive Tpbg knockout mouse line B6;129S5-Tpbg^{tm1Lex}/Mmucd (referred
286 to as TPBG-KO or KO) to analyze the consequences of genetic deletion of TPBG in the retina.
287 Wild type (WT) littermates were used as controls. Expression and localization of TPBG were
288 examined by western blotting and immunofluorescence confocal microscopy (**Figure 1**). As
289 previously reported (Wakeham et al., 2020), the TPBG antibody labels RBC cell bodies, dendrites,
290 and axon terminals in the WT retina, as well as a narrow band in the middle of the IPL
291 corresponding to the processes of TPBG-expressing amacrine cells. TPBG immunoreactivity was
292 absent throughout the KO retina (**Figure 1A**); this was confirmed by immunoblotting (**Figure 1B**)
293 of WT and KO retinal lysates with the TPBG antibody using β-actin as a loading control. Using
294 an antibody against PKCα in WT and TPBG-KO retina, we found no discernable disruption in
295 morphology of RBC dendrites or axon terminals in KO retinas (**Figure 1C-D**).

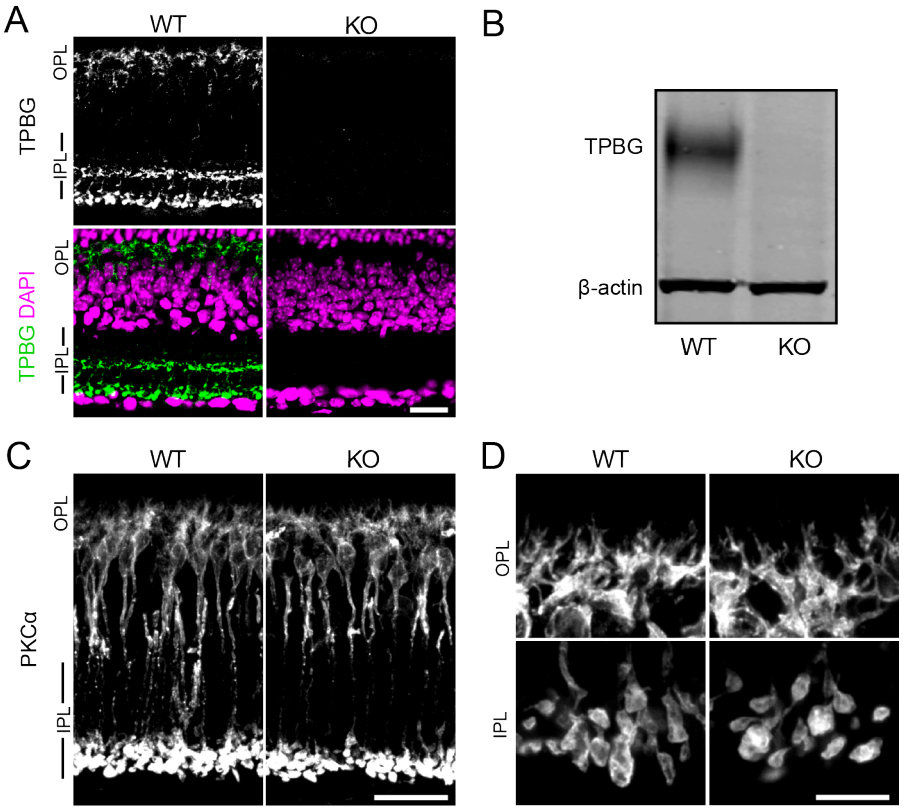

Figure 1: TPBG-KO does not alter gross RBC morphology. **(A)** Immunofluorescence confocal microscopy of WT (left) and TPBG-KO (KO; right) retina sections labeled with an antibody against TPBG (green). The nuclear stain DAPI (bottom; magenta) was used to highlight the neuronal layers of the retina. **(B)** Immunoblot of WT and TPBG-KO (KO) retinal lysates probed for TPBG and β-actin. The two channels were imaged separately and merged. **(C)** Confocal microscopy of WT (left) and TPBG-KO (KO; right) retina sections labeled with an antibody against PKCα. **(D)** Close-up images depicting the OPL (top) and IPL (bottom) for better visualization. For all images, Z-projections of 11 sections were used with a Z-step distance of 0.415 μm for a total thickness of 4.57 μm. Intensity and contrast was adjusted equally across genotypes. OPL: outer plexiform layer; IPL: inner plexiform layer. Scale bars: **(A and C)** 20 μm; **(D)** 10 μm.

Genetic knockout of TPBG alters the scotopic ERG light response

The light response of RBCs is reflected in the b-wave of the dark-adapted (scotopic) full-field electroretinogram (ERG), a commonly-used technique for recording the electrical responses of the whole retina *in vivo*. Different components of the ERG waveform correspond to the activity of specific cell types in the retina. The a-wave is an initial negative deflection corresponding to hyperpolarization of the photoreceptors (Robson & Frishman, 2014), whereas the b-wave, a larger and slower positive deflection, primarily corresponds to the subsequent depolarization of the ON-bipolar cells (Stockton & Slaughter, 1989). Rod driven activity can be isolated by dark-adapting the mouse before testing; therefore, the dark-adapted ERG b-wave represents the activity of RBCs in response to light stimuli.

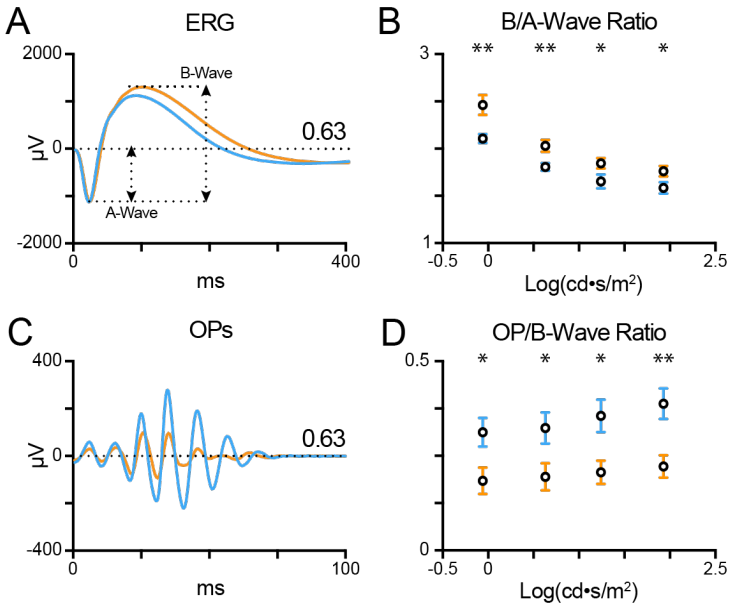

Figure 2: TPBG-KO alters the scotopic ERG after bright stimuli. Scotopic electroretinograms (ERGs) were recorded from dark-adapted WT (blue; n = 12) and TPBG-KO (KO; orange; n = 14) mice after light stimuli (-0.06 to 1.93 log(cd•s/m^2)). **(A)** Example average ERG recordings after light stimuli of 0.63 log(cd•s/m^2). A-wave amplitudes were measured from baseline to the a-wave trough and b-wave amplitudes were measured from the a-wave trough to the b-wave peak. **(B)** Quantification of b-wave amplitudes normalized to a-wave amplitudes. **(C)** Example average oscillatory potentials (OPs) after light stimuli of 0.63 log(cd•s/m^2). **(D)** Quantification of OP amplitudes normalized to b-wave amplitudes. OP amplitudes were measured from the trough to peak of the largest wave. Quantified data is presented as the mean ± SEM. Statistical significance was determined using Welch's *t*-tests; ns: $p > 0.05$; *: $p < 0.05$; ** $p < 0.01$.

We recorded the scotopic ERG light responses in dark-adapted anesthetized WT (blue; *n* = 12) and TPBG-KO (KO; orange; *n* = 14) mice across several stimulus intensities, from dim (-0.06 log(cd•s/m^2)) to bright (1.93 log(cd•s/m^2)). We applied a 60 Hz low-pass filter to remove oscillatory potential (OP) contamination from the ERG a- and b-waves, and a 30-300 Hz Butterworth band-pass filter to isolate OPs for further analysis (**Figure 2 Supplementary Figure 1**). There was no difference in a-wave amplitudes across intensities **(Figure 2: Supplementary Figure 2**), indicating that the KO did not affect the rod photoreceptor light responses, but there was an enlarged b-wave in the TPBG-KO mouse (**Figure 2A**). Because the ERG b-wave is dependent on upstream photoreceptor activation, which is represented by the a-wave, it is common practice for ERG b-wave amplitudes to be normalized to a-wave amplitudes for comparison across animals. The TPBG-KO increased the normalized b-waves (b/a-wave ratio) across the range of stimuli intensities (**Figure 2B**), indicating a larger and more prolonged RBC light response in TPBG-KO mice.

Oscillatory potentials (OPs) are low amplitude, high frequency waves superimposed over the rising phase of the ERG b-wave and observed after bright stimuli. Previous studies indicate that OPs originate from rhythmic activity in the IPL downstream of the bipolar cells (Ogden, 1973).

343 Because the light response of a dark-adapted retina is primarily rod-driven, the OPs are indirectly
344 correlated to RBC output. Therefore, we normalized the OP amplitude by the b-wave amplitude
345 (OP/b-wave ratio) of the corresponding ERG recording. Normalized TPBG-KO OPs were reduced
346 compared to WT (**Figure 2C and D**). TPBG is primarily expressed in RBCs, therefore an effect
347 of TPBG-KO on the OPs is most likely to be due to reduced RBC output onto downstream
348 neurons.
349
350 *TPBG is not required for mGluR6-driven responses in RBC dendrites*
351 We examined the expression and localization patterns of several key pre- and post-
352 synaptic proteins that are are required for synaptic transmission between rod photoreceptors and
353 RBCs. RBCs receive synaptic input from rod photoreceptors via a sign-inverting signal
354 transduction cascade localized to the tips of RBC dendrites. Glutamate released from rod
355 photoreceptors is detected by the group III metabotropic glutamate receptor mGluR6 (Masu et
356 al., 1995; Nakajima et al., 1993; Vardi, Duvoisin, Wu, & Sterling, 2000; Xu et al., 2012), that is
357 negatively coupled to the TRPM1 cation channel (Koike, Numata, Ueda, Mori, & Furukawa, 2010;
358 Koike, Obara, et al., 2010; Morgans et al., 2009; Shen et al., 2009). Thus, a light stimulus relieves
359 TRPM1 tonic inhibition, permitting cation influx and subsequent RBC depolarization.
360

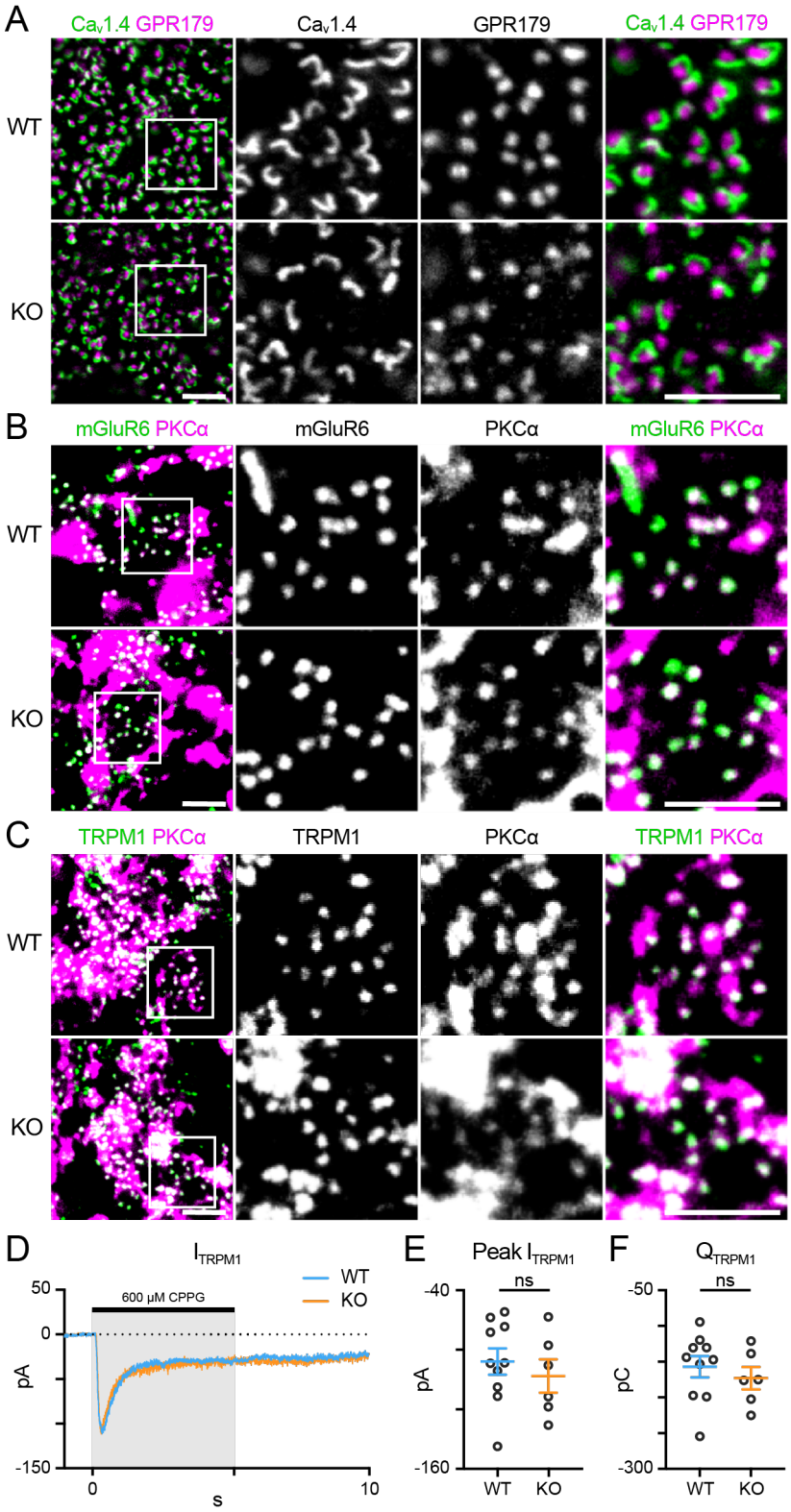

361

362 ***Figure 3: TPBG is not required for mGluR6-driven responses in RBC dendrites.*** **(A-C)** Immunofluorescence
363 confocal microscopy from WT and TPBG-KO whole mount retinas using antibodies against the rod presynaptic calcium

channel ($Ca_v1.4$) and RBC post-synaptic proteins (GPR179, mGluR6, and TRPM1). **(A)** Immunofluorescence labeling of $Ca_v1.4$ (green) and GPR179 (magenta), **(B)** mGluR6 (green) and PKCα (magenta), and **(C)** TRPM1 (green) and PKCα (magenta). Square boxes in the leftmost images indicate regions of interest expanded in the other images. For (**A**), Z-projections of two sections were used with a Z-step distance of 0.297 μm for a total thickness of 0.594 μm. For (**B-C**), Z-projections of ten sections were used for a total thickness of 2.97 μm. All scale bars are 5 μm. **(D-F)** Chemically simulated light responses were recorded in WT (blue; n = 10) and TPBG-KO (KO; orange; n = 6) RBCs following a pulse of 600 μM CPPG for 5 seconds. **(D)** Example CPPG-induced TRPM1 currents. **(E)** Quantification of peak CPPG-induced TRPM1 current (I_{TRPM1}) and **(F)** charge transfer (Q_{TRPM1}) over the five-second duration of the CPPG pulse. Open circles in bar graphs represent single cells and colored bars represent the mean ± SEM. Statistical significance was determined using Welch's t-tests; ns: $p > 0.05$.

First, we looked at the spatial relationship between presynaptic elements in the rod spherule and the tips of the RBC dendrites (**Figure 3A**) using an antibody against the rod L-type Ca^{2+} channel subunit $Ca_v1.4$ to label the horseshoe-shaped active zone and an antibody that labels GPR179 in RBC dendritic tips (Hasan, Ray, & Gregg, 2016). In normal rod-RBC synapses, GPR179 labeling appears as puncta within the concavity of the horseshoe-shaped $Ca_v1.4$ immunofluorescence. We observed no difference in immunofluorescence of RBC dendritic tips in relation to the rod active zones between WT (top) and TPBG-KO (KO; bottom) whole mount retinas. Next, we used immunofluorescence double-labeling with PKCα to compare immunofluorescence of the synaptic proteins mGluR6 and TRPM1, both of which are required for signal transduction in ON-bipolar cells, including RBCs. Co-localization of mGluR6 and TRPM1 puncta with PKCα was indicative of RBC-specific labeling. We observed no difference in mGluR6 (**Figure 3B**) or TRPM1 (**Figure 3C**) immunofluorescence in WT and TPBG-KO RBCs, indicating that TPBG is not required for the accumulation of the mGluR6-TRPM1 signaling complex in RBC dendrites.

Scotopic ERG recordings revealed increased b-waves in TPBG-KO mice (Figure 2) indicating an enhanced light response in KO RBCs. Because the RBC light response is initiated by TRPM1, we compared TRPM1 currents between WT (blue; n = 10) and TPBG-KO (KO; orange; n = 6) RBCs by recording chemically simulated light responses in retinal slices in whole-cell voltage-clamp (**Figure 3D-F**). In this technique, bath application of the mGluR6 agonist L-AP4 maintains the retina in a simulated dark-adapted state, and brief puffs of the mGluR6 antagonist, CPPG, onto the dendrites simulates a light flash and evokes TRPM1 currents (**Figure 3D**). TPBG-KO did not alter the CPPG-induced TRPM1 peak current (**Figure 3E**; WT: -88.24 ± 8.92 pA; KO: -98.04 ± 11.28 pA; Welch's t-test: p = 0.51, t(10.85) = 0.68) or charge transfer (**Figure 3F**; WT: -157.10 ± 47.01 pC; KO: -173.10 ± 38.62 pC; Welch's t-test: p = 0.47, t(12.40) = 0.74). These results suggest that TPBG is not required for the formation of functional rod-RBC synapses and that the larger scotopic ERG b-waves do not reflect enhanced TRPM1 currents in the TPBG-KO.

TPBG is not required for the formation of RBC synaptic ribbons.

Oscillatory potentials are thought to be generated by the inner retina, and RBCs drive the majority of downstream activity under scotopic conditions; thus, the attenuation of scotopic OPs in the TPBG-KO suggests a deficit in RBC output to third-order neurons. Like rods, RBCs signal to downstream cells using ribbon synapses. A depolarized potential entering the axon terminal prompts the opening of L-type voltage-gated Ca^{2+} channels clustered beneath the ribbons and the resulting influx of Ca^{2+} triggers the fusion (exocytosis) of ribbon-tethered synaptic vesicles (von Gersdorff, Vardi, Matthews, & Sterling, 1996). This process requires a close spatial relationship between the Ca^{2+} channels the synaptic ribbons (Jarsky, Tian, & Singer, 2010). We used triple immunofluorescence microscopy to examine the relative localization and expression patterns of the L-type Ca^{2+} channel subunit, $Ca_v1.4$, and the synaptic ribbon protein RIBEYE (**Figure 4**). Because neither $Ca_v1.4$ nor RIBEYE are specific to RBC axon terminals, we isolated RBC-specific immunofluorescence using a binary mask derived from PKCα immunofluorescence to exclude labeling from other bipolar cells in the IPL. $Ca_v1.4$ and RIBEYE show punctate immunofluorescence in RBC axon terminals and are co-localized or closely apposed. We found no difference between WT and TPBG-KO (KO) $Ca_v1.4$ and RIBEYE immunofluorescence patterns. In both conditions, each RIBEYE punctum was closely associated with a $Ca_v1.4$ punctum, suggesting TPBG is not required for active zone formation or maintenance in RBC synaptic terminals and further confirming the absence of morphological changes in TPBG-KO RBCs.

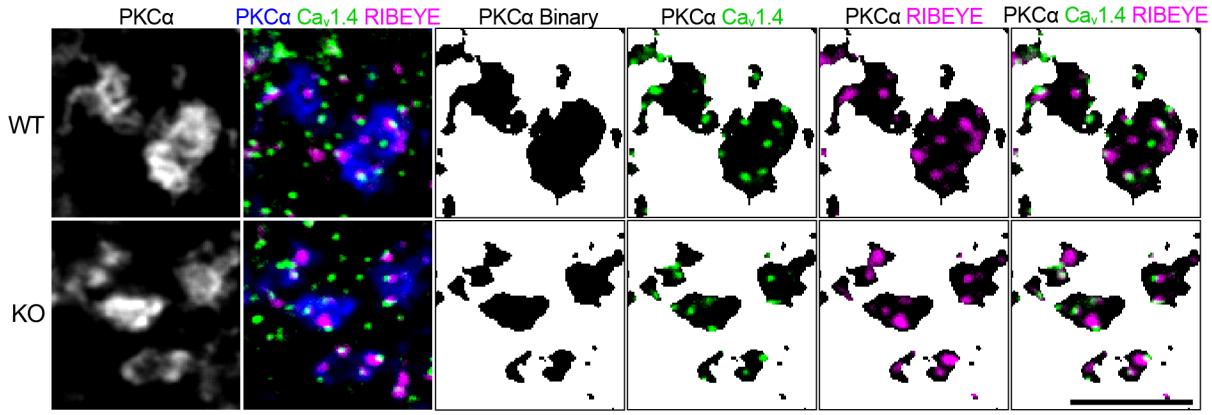

Figure 4: TPBG is not required for the co-localization of synaptic proteins in RBC axon terminals. Triple immunofluorescence confocal microscopy of WT and TPBG-KO (KO) whole mount retinas using antibodies against PKCα (blue), $Ca_v1.4$ (Green) and RIBEYE (magenta). To isolate labeling in RBC axon terminals, binary images were created using the PKCα channel and overlayed over the other two channels to generate binary masks. Z-projections of two sections were used with a Z-step distance of 0.297 μm for a total thickness of 0.547 μm. The scale bar is 5 μm.

431 *TPBG is required for efficient exocytosis in RBC synaptic terminals.*

432 To examine the effect of TPBG-KO on RBC synaptic output, we recorded time-resolved
433 membrane capacitance (C_m) before and after a depolarizing pulse using the "sine + DC" method
434 (Gillis, 2000; Oltedal & Hartveit, 2010). High-resolution membrane capacitance changes (ΔC_m)
435 after a depolarizing pulse strongly correlate with vesicle exocytosis in neuroendocrine cells
436 (Klyachko & Jackson, 2002; Neher & Marty, 1982) and glutamate release from bipolar cell axon
437 terminals (Kim & von Gersdorff, 2016). A sinusoidal voltage command (200 Hz at 30 mV trough-
438 to-peak) was superimposed over the holding voltage of -80 mV and exocytosis was evoked by
439 depolarizing the cell to -10 mV to open the voltage-gated Ca^{2+} channels (**Figure 5:**
440 **Supplementary Figure 1A)**. Membrane capacitance (C_m), membrane resistance (R_m), and series
441 resistance (R_s) were recorded before and after the pulse and ΔC_m was measured as the change
442 in C_m after exocytosis. Changes in R_m and R_s were not correlated with changes in C_m (**Figure 5:**
443 **Supplementary Figure 1B**).

444 C_m measurements in RBCs are complicated by the attenuation and filtering of the
445 sinusoidal voltage command amplitude down their narrow axons (Oltedal & Hartveit, 2010;
446 Oltedal, Veruki, & Hartveit, 2009). We sought to confirm that a low-frequency sinusoidal command
447 reduces attenuation and maximizes RBC C_m changes compared to higher frequencies (**Figure 5:**
448 **Supplementary Figure 1C-F**) using 200 (n = 6), 400 (n = 4), 800 (n = 4), and 1600 (n = 4) Hz
449 commands. We found no difference in the voltage-gated Ca^{2+} current amplitude (I_{Ca}) or charge
450 transfer (Q_{Ca}) across frequencies (not shown), but the ΔC_m (**Figure 5: Supplementary Figure 1C**
451 **and D**; 200 Hz: 41.94 ± 4.95 fF; 400 Hz: 19.13 ± 4.06 fF; 800 Hz: 4.05 ± 2.91 fF; 1600 Hz: -4.23
452 ± 1.40; Brown-Forsythe ANOVA: $p < 0.0001$, 34.12(2.00, 10.87)) and the resting C_m (**Figure 5:**
453 **Supplementary Figure 1E and F**; 200 Hz: 5.97 ± 0.23 pF, 400 Hz: 5.73 ± 0.12 pF, 800 Hz: 4.81
454 ± 0.15 pF, 1600 Hz: 4.04 ± 0.12 pF; Brown-Forsythe ANOVA: $p < 0.0001$, 25.06(3.00, 11.34))
455 were greater at 200 Hz compared to higher frequencies. These supplementary results support
456 our decision to examine exocytosis in RBCs using a 200 Hz "sine + DC" protocol.

457 To examine RBC synaptic vesicle exocytosis, we used whole-cell voltage-clamp to
458 compare WT (blue; n = 6) and TPBG-KO (KO; orange; n = 7) voltage-gated Ca^{2+} currents and
459 subsequent changes in membrane capacitance (**Figure 5**). Cells where C_m, R_m, and R_s were
460 highly correlated were discarded. The synaptic blockers L-AP4, strychnine, TPMPA, and
461 gabazine were used to block spontaneous activity and help increase and stabilize R_m during
462 recordings. The passive properties of R_m (WT: 1.603 ± 0.24 GΩ; KO: 1.630 ± 0.16 GΩ; Welch's
463 t-test: $p = 0.93$, $t(8.84) = 0.097$) and R_s (WT: 50.54 ± 2.33 MΩ; KO: 49.61 ± 1.91 MΩ; Welch's t-

test: p = 0.76, t(10.16) = 0.31) were not different between WT and TPBG-KO RBCs. As long as R_m is significantly greater than R_s, ΔC_m should be a faithful approximation of overall exocytosis (Gillis, 2000).

TPBG-KO had no effect on the voltage-gated Ca^{2+} currents (**Figure 5B and C**; WT: -74.99 ± 4.49 pA, KO: -74.24 ± 3.41 pA; Welch's *t*-test: $p = 0.90$, $t(9.73) = 0.13$) or charge transfer (**Figure 5D**; WT: -7.0 ± 0.38 pC, KO: -6.7 ± 0.33 pC; Welch's *t*-test: $p = 0.57$, $t(10.43) = 0.58$). However, TPBG-KO resulted in a reduction in ΔC_m compared to WT (**Figure 5E and F**; WT: 41.94 ± 4.95 fF, KO: 25.90 ± 3.91 fF; Welch's *t*-test: $p = 0.029$, $t(9.95) = 2.55$), suggesting a decrease in synaptic vesicle exocytosis in the KO. Most interestingly, the efficiency of exocytosis (the ratio of ΔC_m per unit Q_{Ca}) is also reduced in the KO (**Figure 5G**; WT: 5.93 ± 0.50 fF/-pC, KO: 3.76 ± 0.44 fF/-pC; Welch's *t*-test: $p = 0.0077$, $t(10.52) = 3.28$), indicating that TPBG-KO alters the efficiency of RBC vesicle exocytosis without changing Ca^{2+} influx.

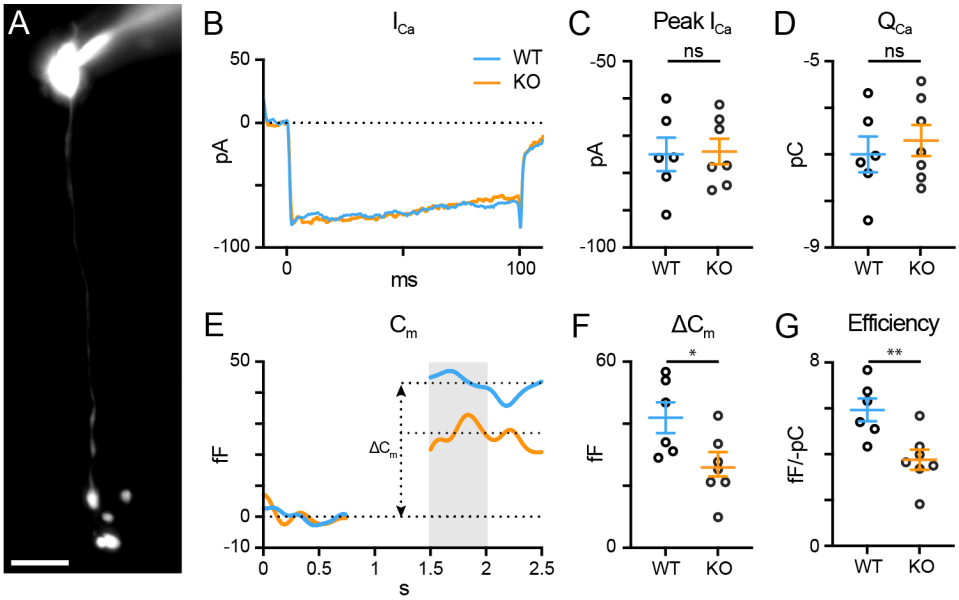

Figure 5: TPBG is required for efficient synaptic vesicle release in RBC axon terminals. Whole-cell voltage-clamp recordings were performed in WT (blue; *n* = 6) and TPBG-KO (KO; orange; *n* = 7) RBCs. **(A)** Epifluorescence micrograph of an RBC filled with Alexa Fluor 594 Hydrazide after patch-clamp recording. RBCs were patched and cell type was verified *post-hoc* using epifluorescence microscopy. The scale bar is 10 μm. **(B)** Average voltage-gated Ca^{2+} current traces recorded after a depolarizing pulse from -80 mV to -10 mV for 100 ms. **(C)** Quantification of peak voltage-gated Ca^{2+} current amplitudes (I_{Ca}) and **(D)** charge transfer (Q_{Ca}) over the duration of the pulse. **(E)** Average membrane capacitance (C_m) recordings using a 200 Hz sine + DC protocol. ΔC_m was measured as the difference between baselined resting C_m before and after the depolarizing pulse. Data immediately after the pulse was excluded until C_m stabilized. The gray bar represents the region across which C_m values were averaged. **(F)** Quantification of ΔC_m. **(G)** Quantification of exocytosis efficiency calculated as the absolute value of the change in C_m per unit Q_{Ca}. Ames medium was supplemented with 1 mM $CaCl_2$ and (in μM): 0.5 strychnine, 3 gabazine, 50 TPMPA, and 4 L-AP4. Open circles in bar graphs represent single cells and bars represent the mean ± SEM. Statistical significance was determined using Welch's *t*-tests; ns: $p > 0.05$; *: $p < 0.05$; **: $p < 0.01$.

492 *TPBG does not alter RBC input resistance or excitability*

493

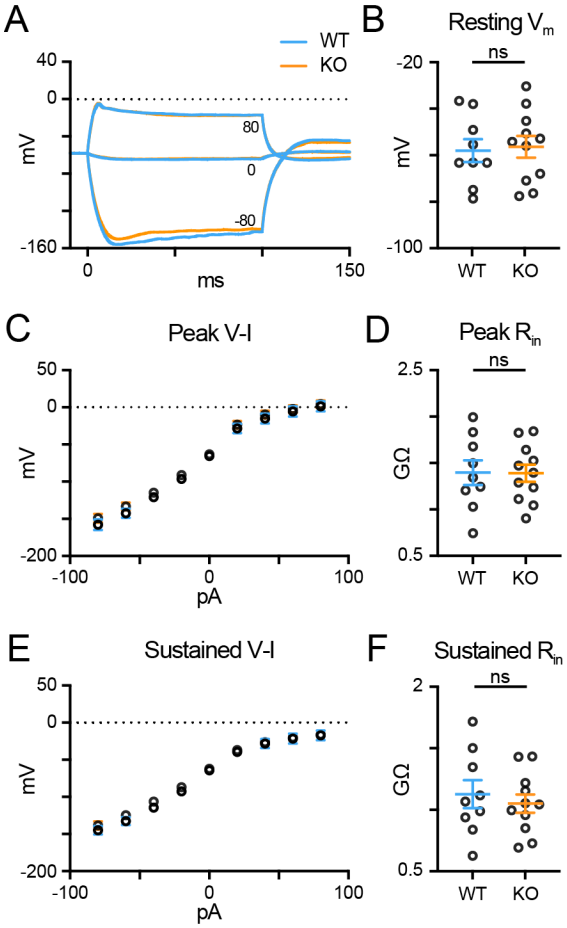

494

495 ***Figure 6: TPBG does not alter RBC input resistance or excitability***. Whole-cell current-clamp recordings in WT
496 (blue; *n* = 9) and TPBG-KO (KO; orange; *n* = 11) RBCs were used to construct a current-voltage relationship and
497 calculate input resistance (R_{in}). A current injection protocol from -80 pA to 80 pA in 20 pA steps was used with a K-
498 gluconate-based internal solution. **(A)** Average voltage traces following -80 pA, 0 pA, and 80 pA current injections for
499 100 ms. **(B)** Resting membrane voltages recorded immediately after entering current clamp mode. **(C)** A plot of the
500 voltage-current (V-I) relationship measured at the peak voltage during current injections. **(D)** Quantification of peak R_{in}.
501 **(E)** A plot of the sustained V-I relationship measured as the average voltage calculated over the last 10 ms of the
502 current pulse. **(F)** Quantification of the sustained R_{in}. Peak and sustained R_{in} values were calculated by measuring the
503 slope of the linear portion of the V-I curves (from -40 to 40 pA). Ames medium was supplemented with 1 mM $CaCl_2$
504 and (in μM): 0.5 strychnine, 3 gabazine, 50 TPMPA, and 4 L-AP4. For V-I curves, open circles represent the mean and
505 error bars represent SEM. For quantification, open circles represent single cells and bars represent the mean ± SEM.
506 Statistical significance was determined using Welch's *t*-tests; ns: $p > 0.05$.

507

508 TPBG-KO amplifies the RBC light response and reduces synaptic vesicle exocytosis,
509 suggesting that TPBG-KO may reduce the gain of RBC synaptic release by shifting RBC
510 excitability. To compare the excitability between WT (blue; *n* = 9) and TPBG-KO (KO; orange; *n*
511 = 11) RBCs, we used current injections (from -80 to 80 pA in 20 pA intervals) in whole-cell current-
512 clamp mode to construct voltage-current relationships and calculate the peak and sustained input
513 resistances (R_{in}). For these experiments, we used the synaptic blockers L-AP4, strychnine,

514 TPMPA, and gabazine to isolate RBC-specific voltage responses. **Figure 6A** shows voltage
515 responses after representative current injections of -80 pA, 0 pA, and +80 pA. The resting
516 membrane potential (V_m) was unchanged in the KO (**Figure 6B**; WT: -58.02 ± 4.91 mV, KO: -
517 56.35 ± 4.66 mV; Welch's *t*-test: $p = 0.81$, $t(17.53) = 0.25$). We found no difference in peak (**Figure**
518 **6C and D**; WT: 1.40 ± 0.13 GΩ, KO: 1.39 ± 0.09 GΩ; Welch's *t*-test: $p = 0.97$, $t(14.94) = 0.04$) or
519 sustained R_{in} (**Figure 6E and F**; WT: 1.13 ± 0.11 GΩ, KO: 1.05 ± 0.07 GΩ; Welch's *t*-test: $p =$
520 0.58, $t(14.28) = 0.56$) between the WT and KO RBCs. These results indicate that a shift in R_{in} and
521 RBC excitability in the TPBG-KO is do not explain the reduced exocytosis.
522
523 *TPBG-KO reduces reciprocal inhibitory feedback*
524 RBCs drive retinal output via glutamate release into the IPL, which stimulates Ca^{2+}-
525 permeable AMPA receptors in downstream AII amacrine cells (AII-ACs). RBC glutamate release
526 is also detected by A17 amacrine cells (A17-ACs), which when depolarized, release GABA back
527 onto RBC synaptic terminals where it is sensed by $GABA_A$ and $GABA_A\rho$ (also called $GABA_C$) Cl^-
528 channels (**Figure 7A**). An influx of Cl^- into the axon terminal through open GABA channels
529 provides inhibitory feedback by hyperpolarizing the RBC and shaping further RBC glutamate
530 release (Chávez, Grimes, & Diamond, 2010; Chávez, Singer, & Diamond, 2006; Euler & Masland,
531 2000; E. Hartveit, 1996; Espen Hartveit, 1999; Singer & Diamond, 2003). Each RBC forms a dyad
532 synapse with one AII-AC and one A17-AC (Famiglietti & Kolb, 1975; Grimes, Zhang, Graydon,
533 Kachar, & Diamond, 2010; McGuire, Stevens, & Sterling, 1984; Raviola & Dacheux, 1987). As
534 A17-mediated reciprocal feedback is driven by RBC glutamate release, the inhibitory feedback
535 currents in the RBCs are an indirect measure of glutamate release from RBCs and would be
536 expected to be reduced concomitantly with reduced RBC exocytosis in the TPBG-KO.

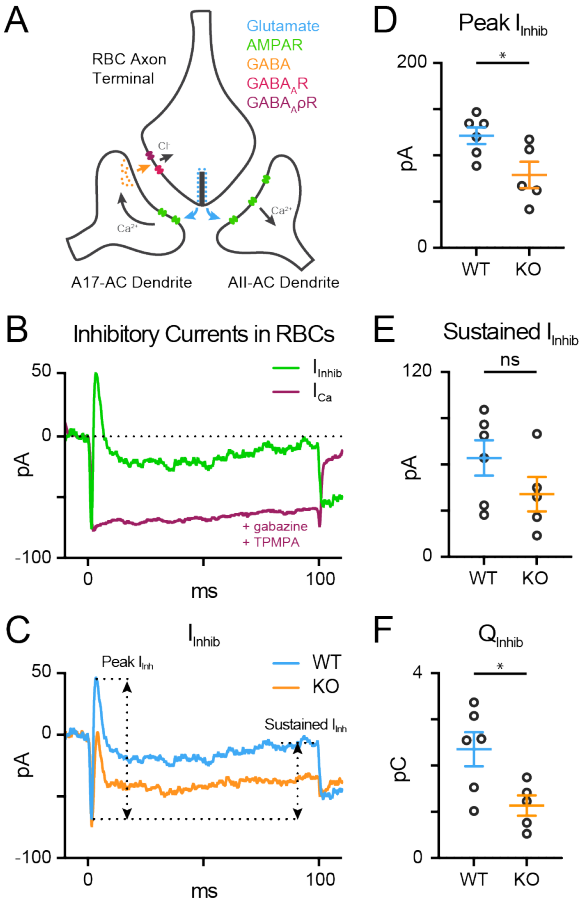

Figure 7: TPBG-KO reduces reciprocal inhibitory feedback. **(A)** The dyad synapse arrangement between one RBC, one AII-AC, and one A17-AC in the IPL. Glutamate release by RBCs is detected by Ca^{2+}-permeable AMPA receptors (AMPARs) in AII-AC and A17-AC dendrites. A17-ACs then release GABA back onto the synaptic cleft which is sensed by $GABA_A$ receptors ($GABA_A$Rs) and $GABA_A\rho$ receptors ($GABA_A\rho$Rs) in the RBC axon terminals. **(B)** Inhibitory currents are superimposed over voltage-gated Ca^{2+} currents. Reciprocal feedback in RBCs was evoked with a 100 ms depolarizing pulse from -80 mV to -10 mV. In the absence of GABA receptor blockers, this depolarizing pulse elicits an inward voltage-gated Ca^{2+} current that is quickly subsumed by outward inhibitory currents (I_{Inhib}; green). These outward currents are abolished by the application of the GABA receptor blockers gabazine and TPMPA (I_{Ca}; magenta). **(C)** Average whole-cell patch-clamp recordings from WT (blue; n = 6) and TPBG-KO (KO; orange; n = 5) RBCs to compare reciprocal inhibitory feedback after a depolarizing pulse from -80 mV to -10 mV for 100 ms. Current amplitudes and charge transfers were measured from a baseline set to the maximum inward current following depolarization (exemplified by the horizontal dotted line), which is very similar to the voltage-gated Ca^{2+} currents amplitude in **B**. **(D)** Quantification of peak inhibitory current measured from baseline. **(E)** Quantification of the sustained inhibitory current measured from baseline to the average current over the last 10 ms of the depolarizing pulse. **(F)** Quantification of the charge transfer measured from baseline over the duration of the 100 ms stimulus. Ames medium was supplemented with 1 mM $CaCl_2$, 0.5 μM strychnine and 4 μM L-AP4. Open circles in bar graphs represent single cells and bars represent the mean ± SEM. Statistical significance was determined using Welch's *t*-tests; ns: $p > 0.05$; *: $p < 0.05$.

To test the hypothesis that reduced RBC glutamate release results in smaller inhibitory feedback currents in the TPBG-KO, we used whole-cell voltage-clamp to examine the reciprocal inhibitory response to a depolarizing pulse from -80 mV to -10 mV for 100 ms in WT (blue; n = 6) and TPBG-KO (KO; orange; n = 5) RBCs. L-AP4 was used to block spontaneous excitatory inputs and strychnine was used to block glycinergic inhibition. In the absence of GABA receptor blockers, two outward currents can be seen superimposed on the evoked voltage-gated Ca^{2+} current

562 (**Figure 7B**): a large, fast-activating, fast-inactivating current (labeled Peak I_{Inhib}) and a smaller
563 slowly-activating, non-inactivating current (labeled Sustained I_{Inhib}). Since these two currents likely
564 have different sources, we quantified their amplitudes separately. We found that TPBG-KO
565 reduced the peak inhibitory feedback current (**Figure 7C and D**; WT: 121.20 ± 8.83 pA; KO: 78.83
566 ± 14.23 pA; Welch's t-test: p = 0.04, t(6.92) = 2.52) whereas the sustained current did not change
567 in the KO (**Figure 7C and E**; WT: 64.22 ± 11.52 pA; KO: 40.74 ± 11.16; Welch's t-test: p = 0.18,
568 t(8.94) = 1.46). Lastly, the charge transfer across the duration of the stimulus was also reduced
569 in the TPBG-KO compared to WT (**Figure 7F**; WT: 2.35 ± 0.37 pC; KO: 1.13 ± 0.22 pC; Welch's
570 t-test: p = 0.022, t(7.83) = 2.83). This supports our previous result that the TPBG-KO suppresses
571 RBC vesicle exocytosis and glutamate release (see **Figure 5F**).
572

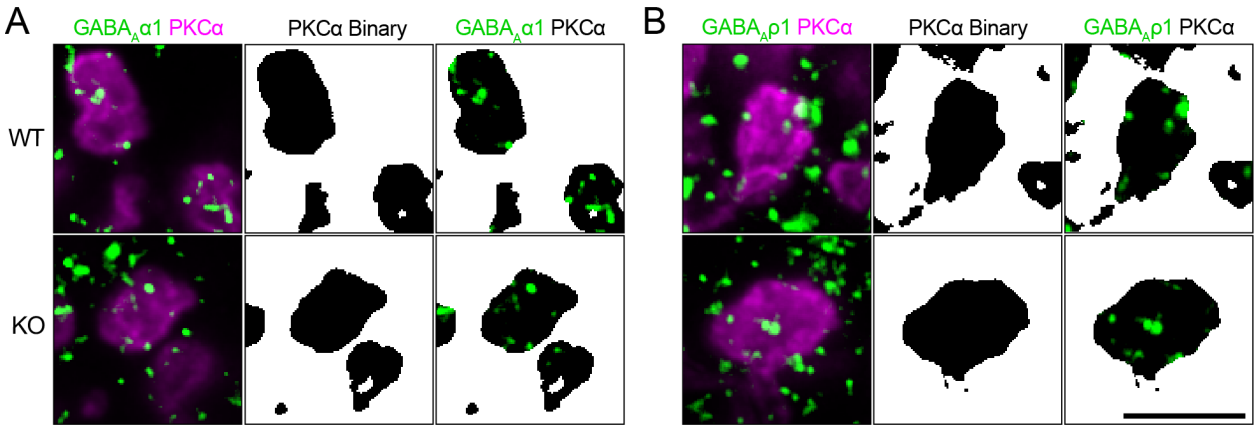

573
574
575 ***Figure 8: TPBG is not required for localization of GABA receptor immunofluorescence to RBC axon terminals***.
576 Immunofluorescence confocal microscopy of WT and TPBG-KO (KO) whole mount retinas using an antibody against
577 PKCα (magenta) and antibodies against either the GABA$_A$α1 subunit (**A**; green) or the GABA$_A$ρ1 subunit (**B**; green).
578 To isolate labeling in RBC axon terminals, binaries were created using the PKCα channel and overlayed over the other
579 channels to generate binary masks. For all images, Z-projections of two sections were used with a Z-step distance of
580 0.297 μm for a total thickness of 0.547 μm. Scale bar is 5 μm.
581

582 It is possible that reciprocal feedback is altered in TPBG-KO due to disrupted expression
583 or clustering of GABA receptors in RBC axon terminals. RBCs express both GABA$_A$α1 and
584 GABA$_A$ρ1 subunits in their axon terminals (Fletcher, Koulen, & Wässle, 1998; Palmer, 2006). To
585 see whether TPBG-KO alters GABA receptor expression patterns, we used double
586 immunofluorescence labeling of WT and TPBG-KO whole mount retinas using an antibody
587 against PKCα and antibodies against GABA$_A$α1 and GABA$_A$ρ1 receptor subunits (**Figure 8**). As
588 previously, we isolated RBC axon terminal-specific labeling using a binary mask derived from
589 PKCα immunofluorescence. We did not observe any major differences in immunofluorescence
590 between WT (top) and TPBG-KO (KO; bottom) retinas labeled against either GABA$_A$α1 (**Figure**

591 **8A**) or $GABA_A\rho1$ (**Figure 8B**), indicating that impaired GABA receptor expression is likely not
592 reducing inhibitory feedback. Taken together, our data supports the conclusion that TPBG is
593 required for efficient synaptic vesicle exocytosis and glutamate release from RBC axon terminals.
594
595 **Discussion**
596 In this study, we characterized the functional consequences of genetic knockout of TPBG
597 in the mouse retina using immunofluorescence and electrophysiological approaches. TPBG-KO
598 did not alter gross RBC morphology in the OPL or IPL as PKCα-labeled RBC dendrites and axon
599 terminals appear normal in both conditions. Because TPBG is localized to both the dendrites and
600 axon terminals of RBCs (Wakeham et al., 2020), we sought to examine the effect of TPBG-KO
601 on the RBC synaptic structure and physiology in both compartments. Though ERG b-waves were
602 larger in the TPBG-KO, dendritic TRPM1 currents activated by CPPG did not change. In contrast
603 to the larger b-waves, the scotopic OPs were smaller in the KO, suggesting changes in RBC
604 ribbon synapse function. Accordingly, time-resolved C_m measurements and whole-cell recording
605 indicated that synaptic vesicle exocytosis and GABAergic feedback are reduced at TPBG-KO
606 RBC synapses. Importantly, we did not detect differences in presynaptic voltage-gated Ca^{2+}
607 current amplitude or changes in Ca^{2+} channel, GABA receptor, or RIBEYE expression and
608 localization. We propose that TPBG plays an important role in fine tuning the synaptic architecture
609 of RBC ribbon synapses to increase exocytosis efficiency.
610
611 *TPBG and RBC dendrites*
612 We found that TPBG is not required for the normal insertion of RBC dendritic tips inside
613 rod spherules or for normal depolarizing currents through TRPM1 cation channels. Our
614 immunofluorescence and electrophysiological examination of RBC dendrites suggest that TPBG
615 is not essential for basic synaptic function in that compartment. That being said, TPBG
616 immunofluorescence reveals that large amounts of TPBG are present in RBC dendrites,
617 suggesting some role in dendritic development or physiology.
618 TPBG regulates dendritic arborization in mouse olfactory bulb granule cells (Yoshihara et
619 al., 2012). In these neurons, TPBG-KO reduced dendritic branching and dendritic migration to
620 synaptic targets. Lentiviral overexpression of TPBG increased dendritic branching complexity and
621 restored dendritic arborization deficits induced by nasal occlusion. In the retina, TPBG may also
622 regulate RBC dendritic branching complexity in the OPL. TPBG is a known regulator of Wnt
623 signaling (He et al., 2015; Kagermeier-Schenk et al., 2011), which is required for functional
624 synaptic targeting and OPL lamination in RBCs, therefore TPBG may promote RBC dendritic

625 development through control of the Wnt pathway (Tsuboi, 2020). We didn't detect a structural or
626 physiological phenotype in RBC dendrites, but thorough evaluation of RBC dendritic maturation
627 and branching using sparse labeling techniques might reveal a more subtle effect of TPBG-KO
628 on dendritic architecture.
629
630 *TPBG and RBC synaptic vesicle exocytosis*
631 We found a reduction in the OPs isolated from scotopic ERG recordings in TPBG-KO
632 mice, which we interpret as evidence for decreased RBC output to third-order neurons. While the
633 specific cell types that contribute to OP generation are unknown, it is generally accepted that OPs
634 stem from rhythmic activity in the IPL (Wachtmeister, 1998). Early studies implicated interactions
635 between bipolar cell axon terminals, amacrine cell processes, and ganglion cell dendrites as
636 potential generators of the OPs (Ogden, 1973). Intravitreal injections of glycine into rabbit retinas
637 resulted in morphological changes in many ACs and disappearance of the OPs from the ERG
638 (Korol, Leuenberger, Englert, & Babel, 1975) while application of neurotoxic kainate to ganglion
639 cell dendrites diminishes OP amplitude (Vaegan & Millar, 1994). A more recent study
640 unequivocally implicates multiple distinct generators in the production of early, intermediate, and
641 late OP peaks (Dong, Agey, & Hare, 2004). The use of APB and CNQX to block synaptic inputs
642 to ON and OFF-bipolar cells significantly diminished intermediate and later OPs but left early OPs
643 intact, suggesting that early OPs are generated by photoreceptors. Intermediate and late OPs
644 have differential sensitivity to tetrodotoxin, which abolished only late OPs, indicating that
645 intermediate OPs are generated by action-potential-independent interactions and late OPs are
646 generated by action-potential-dependent ones (Dong et al., 2004). Our OP data shows a much
647 larger attenuation of TPBG-KO OP amplitude in intermediate and late OPs compared to early
648 ones. Thus, the results of these studies support our conclusion that reduced scotopic OPs are
649 likely due to suppressed rhythmic activity of third-order neurons due to reduced RBC glutamate
650 release.
651 By simultaneously recording the presynaptic voltage-gated Ca^{2+} currents and subsequent
652 membrane capacitance changes evoked by RBC depolarization, we showed that TPBG-KO
653 reduced exocytosis compared to WT RBCs despite no change in presynaptic Ca^{2+} currents,
654 indicating reduced exocytosis efficiency in the TPBG-KO compared to WT RBCs. The Ca^{2+}
655 current amplitudes we recorded (-75 pA) following a depolarizing step are significantly larger than
656 those previously reported (-30 pA by Protti & Llano, 1998 and -20 pA by Singer & Diamond, 2003).
657 We also recorded larger C_m jumps (42 fF in WT) than those reported from dissociated RBCs (30
658 fF in Zhou, Wan, Thakur, & Heidelberger, 2006). We believe these differences can be attributed

659 to higher recording temperatures (33° C vs 21° C). With a mean resting C_m of 5.97 pF and a
660 mean R_s of 50.04 MΩ, we can calculate an average voltage-clamp speed of 298.74 μs –
661 sufficiently fast to clamp the membrane to a 200 Hz sine wave with a 5 ms period. The smaller
662 capacitance jumps in the TPBG-KO, despite the same Ca^{2+} currents as in WT, suggests that
663 calcium influx is not as tightly coupled to the synaptic vesicle exocytosis in the TPBG-KO, resulting
664 in reduced exocytosis efficiency.

665 Exocytosis efficiency is calculated as the exocytosis per unit Ca^{2+} charge transfer. We
666 calculated an exocytosis efficiency of approximately 6 fF/pC (**Figure 5G**) in adult WT mouse
667 RBCs after a 100 ms depolarizing pulse at 33° C. In adult vertebrate auditory hair cells, which
668 also form ribbon synapses, similar exocytosis efficiencies of 5 to 6 fF/pC have been reported after
669 100 ms pulses (Chen & von Gersdorff, 2019; Moser et al., 2020). Like bipolar cells, hair cell ribbon
670 synapses operate via nanodomain coupling between Ca^{2+} channels and docked vesicles (Jarsky
671 et al., 2010). However, exocytosis efficiency usually increases with shorter depolarizing pulses
672 and can be as high as 16 to 20 fF/pC at immature calyx of Held axon terminals after a 1 ms pulse.
673 The calyx of Held axon terminals contain conventional active zones, not synaptic ribbons, and
674 operate via Ca^{2+} microdomains where Ca^{2+} influx can trigger and vesicle exocytosis from greater
675 distances (Kushmerick, Renden, & von Gersdorff, 2006). Further studies will be required to verify
676 the relationship between TPBG and nanodomain coupling at RBC ribbon synapses.
677

678 *TPBG and synaptic ribbon proteins*

679 Neurotransmitter release from synaptic ribbons can be simplified into three major steps:
680 synaptic docking, Ca^{2+} influx and its detection by Ca^{2+} sensors, and Ca^{2+}-dependent fusion of
681 synaptic vesicles with the presynaptic membrane (Dieck & Brandstätter, 2006; Morgans, 2000).
682 These are all potential points at which TPBG may be supporting efficient vesicle release from
683 RBCs. Vesicle accumulation and transport in RBC synaptic terminals is dependent on F-actin
684 polymerization and is regulated by PKCα (Berglund, Midorikawa, & Tachibana, 2002; Doussau &
685 Augustine, 2000; Job & Lagnado, 1998; Minami, Berglund, Sakaba, Kohmoto, & Tachibana, 1998;
686 Tachibana, 1999). We originally identified TPBG as a PKCα-dependent phosphoprotein
687 (Wakeham et al., 2019); thus, it is possible that PKCα controls vesicle docking via actin dynamics
688 in RBC axon terminals through TPBG.

689 The tight temporal control of vesicle release that is a trademark of synaptic ribbons
690 requires nanodomain-coupling between L-type voltage-gated Ca^{2+} channels and Ca^{2+} binding
691 proteins that trigger synaptic vesicle fusion (Balakrishnan et al., 2015; Eggermann, Bucurenciu,
692 Goswami, & Jonas, 2012; Jarsky et al., 2010). Synaptic ribbons are primarily composed of the

693 scaffold protein RIBEYE and are anchored to the presynaptic active zone by a number of
694 cytoskeletal anchoring proteins, including Bassoon and Piccolo (Zanazzi & Matthews, 2009). We
695 did not observe a difference in RIBEYE immunofluorescence in WT and TPBG-KO axon
696 terminals, but immunofluorescence does not have the resolution to confirm the correct localization
697 or orientation of the ribbon at the active zone. If TPBG is required for correct localization of the
698 ribbon, exocytosis efficiency may be significantly disrupted in KO RBCs. $Ca_v1.4$ and RIBEYE
699 appear co-localized by immunofluorescence in both WT and TPBG-KO RBC axon terminals, but
700 a small disruption of this tight coupling might not be detected with immunofluorescence and could
701 have a large effect on glutamate release by slowing the accumulation of Ca^{2+} at the sensor.
702 Nanodomain coupling likely depends on a close spatial relationship between the L-type channels
703 and the vesicle release machinery, yet it is not fully known how this clustering is achieved in
704 RBCs. It is possible that TPBG facilitates Ca^{2+} channel clustering or association between the
705 channels and the ribbon such that, in its absence, normal nanodomain coupling is disrupted and
706 synaptic vesicle fusion is reduced.
707 Lastly, TPBG could be involved in the mechanics of synaptic vesicle fusion. Vesicle fusion
708 in RBC synapses is accomplished by Ca^{2+}-sensitive synaptotagmins and a complex of three
709 SNARE proteins: synaptobrevin, SNAP-25, and syntaxin 3. Synaptobrevin is an integral
710 membrane protein of the synaptic vesicles, but SNAP-25 and syntaxin 3 are localized to the
711 presynaptic membrane (Morgans, 2000; Morgans, Brandstätter, Kellerman, Betz, & Wässle,
712 1996). Other proteins implicated in vesicle priming and fusion at ribbon synapses are RIM1,
713 Munc13, and CAPS proteins (Moser et al., 2020). These proteins are critical for vesicle fusion
714 and TPBG could interact with them to regulate vesicle exocytosis from RBC synapses.
715
716 *TPBG and reciprocal feedback inhibition*
717 To confirm that the TPBG-KO reduces RBC vesicle fusion and glutamate release, we
718 compared GABAergic feedback inhibition between WT and TPBG-KO RBCs. We found
719 attenuation of peak inhibitory currents and inhibitory charge transfer in the TPBG-KO. With
720 glycinergic inhibition blocked by strychnine, the primary remaining source of feedback inhibition
721 in RBCs is A17-mediated GABAergic reciprocal feedback. GABA released from A17-ACs is
722 sensed by two kinetically distinct ionotropic GABA receptors in RBC axon terminals: $GABA_A$ and
723 $GABA_A\rho$ (Fletcher et al., 1998). $GABA_A$ receptor-mediated current is rapidly-activating, while
724 $GABA_A\rho$-mediated current is slowly-activating (Grimes et al., 2015). We detected two different
725 inhibitory components: a large, quickly-inactivating current and a smaller sustained one. Though
726 we did not pharmacologically isolate each current, the kinetics of the inhibitory currents suggest

727 that peak I_{Inhib} is likely mediated by $GABA_A$ receptors and sustained I_{Inhib} is likely mediated by
728 $GABA_A\rho$ receptors.
729 GABAergic reciprocal feedback from A17-ACs might be altered if GABA receptor
730 expression or localization was disrupted by TPBG-KO. $GABA_A$ receptors are large pentameric ion
731 channels usually containing α, β, and γ subunits. Early work indicates that RBC axon terminals
732 express $GABA_A\alpha1$, $\alpha3$, and $\gamma2$ receptor subunits (Fletcher et al., 1998), but a recent study found
733 that the $\alpha1$ subunit dominates in adult mice (Sinha et al., 2021). $GABA_A\rho$ receptors contain only
734 ρ subunits (Fletcher et al., 1998). Therefore, we used antibodies against $GABA_A\alpha1$ and $GABA_A\rho1$
735 to visualize $GABA_A$ and $GABA_A\rho$ receptor localization and an antibody against PKCα to isolate
736 RBC-specific axon terminals. We did not detect any difference in GABA receptor
737 immunofluorescence in RBC axon terminals between WT and TPBG-KO, indicating that reduced
738 GABAergic feedback is likely not due to disrupted GABA receptor localization.
739 We found that TPBG-KO increased scotopic ERG b-waves, suggesting an increase in
740 RBC depolarization. The scotopic ERG b-wave is initiated by current through TRPM1 non-specific
741 cation channels in the RBC dendrites. Yet, we did not find any difference in CPPG-induced
742 TRPM1 currents between WT and TPBG-KO retinas. The scotopic b-wave is also shaped by RBC
743 inhibition. Pharmacological studies show that blocking inhibitory currents from third-order neurons
744 changes the scotopic b-wave. In particular, injections of a $GABA_A$ antagonist (bicuculline) or a
745 $GABA_A\rho$ antagonist (TPMPA) into the IPL significantly increases the amplitude and duration of
746 the scotopic b-wave (Dong & Hare, 2000, 2003), suggesting that GABAergic feedback from A17-
747 ACs contributes to the shape of the RBC light response. We conclude that the enlarged ERG b-
748 wave in the TPBG-KO is due to reduced inhibitory feedback onto the RBC terminals, secondary
749 to reduced RBC glutamate release by the RBC.
750
751 *Summary*
752 Our findings show that genetic deletion of TPBG attenuates scotopic ERG oscillatory
753 potentials, synaptic vesicle exocytosis from RBCs, and reciprocal feedback onto RBCs. We
754 propose that TPBG is essential for the development or function of RBC ribbon synapses. Further
755 evaluation of TPBG is critical for producing a more comprehensive understanding of its role in
756 fine-tuning RBC synaptic physiology.
757
758
759
760

Figure Supplements

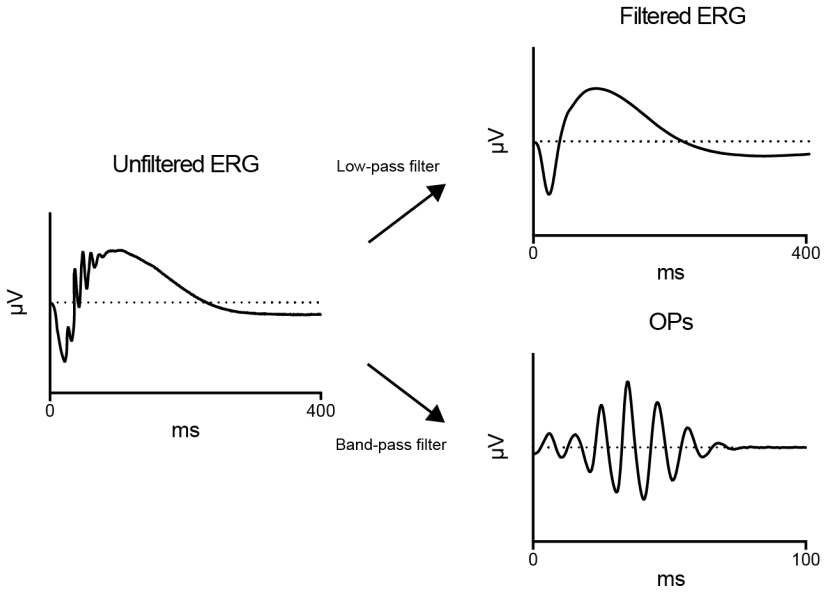

Figure 2: Supplementary Figure 1: ERG filtering to isolate a- and b-waves and OPs. After baselining the raw, unfiltered ERG traces, a 60 Hz low-pass filter was used to remove OPs to better visualize the a- and b-waves (**top right**). A 30-300 Hz Butteworth band-pass filter was used to isolate OPs from the ERG for quantification (**bottom right**).

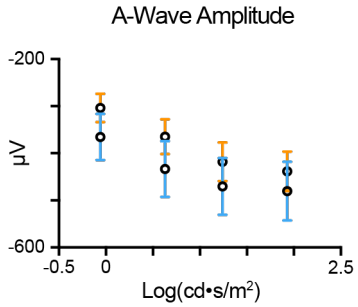

Figure 2: Supplementary Figure 2: TPBG-KO does not alter the scotopic ERG a-wave. Quantification of a-wave amplitudes recorded after light stimuli (-0.06 to 1.93 log(cd•s/m^2)). A-waves are measured from baseline to the a-wave trough. Data is presented as the mean ± SEM.

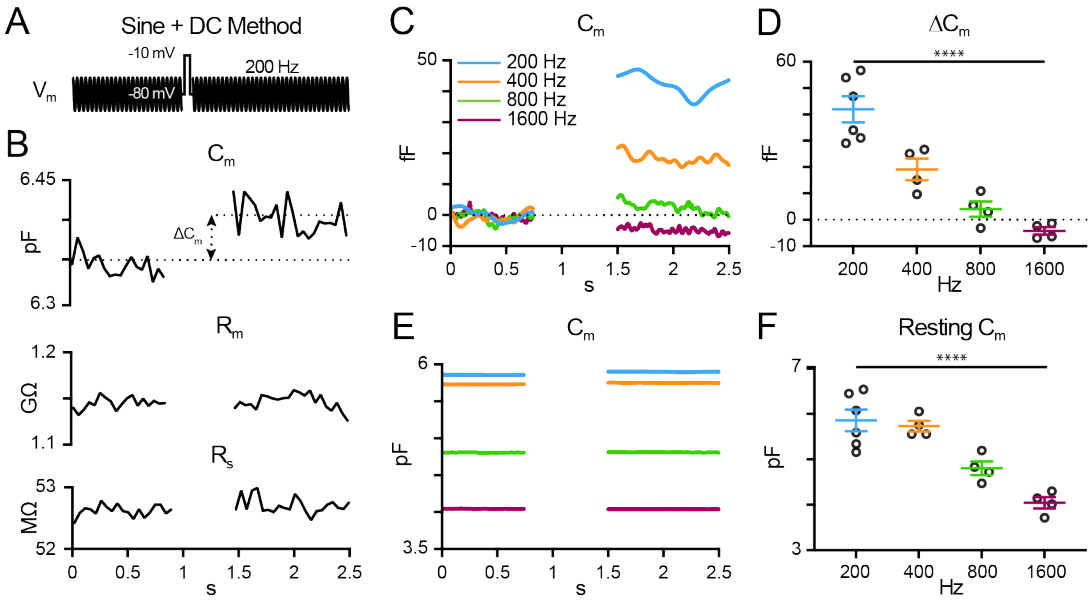

Figure 5: Supplementary Figure 1: Measuring membrane capacitance in RBCs. **(A)** Whole-cell voltage-clamp capacitance recordings were made using the "sine + DC" method. A sinusoidal voltage command (200 Hz at 30 mV trough-to-peak) was superimposed on the holding potential of -80 mV. Membrane capacitance (C_m), membrane resistance (R_m), and series resistance (R_s) were recorded before and after a depolarizing pulse from -80 mV to -10 mV for 100 ms. **(B)** A sample recording from a WT RBC using the sine + DC method as described. The change in membrane capacitance (ΔC_m) was measured as the difference between the C_m before and after the depolarizing pulse. Changes to R_m (middle) and R_s (bottom) were small and do not correlate with changes in C_m. **(C)** Average baseline-subtracted C_m recordings using 200 Hz (blue; n = 6), 400 Hz (orange; n = 4), 800 Hz (green; n = 4), or 1600 Hz (magenta; n = 4) sinusoidal voltage commands in WT RBCs. Data for the 200 Hz condition was reused from WT in Figure 4. Traces with higher frequencies were resampled to 200 Hz for ease of comparisons. **(D)** Quantification of ΔC_m. **(E)** Average C_m recordings and **(F)** quantification of resting C_m across frequencies. Resting C_m was measured before the depolarizing pulse. Open circles in bar graphs represent single cells and bars represent the mean ± SEM. Statistical significance was determined using Brown-Forsythe ANOVA tests; ****: $p < 0.0001$.

785 **References**

786

787 Agosto, M. A., & Wensel, T. G. (2020). LRRTM4 is a member of the transsynaptic complex
788 between rod photoreceptors and bipolar cells. *Journal of Comparative Neurology*, *529*(1),
789 221–233. doi: 10.1002/cne.24944

790 Balakrishnan, V., Puthussery, T., Kim, M.-H., Taylor, W. R., & von Gersdorff, H. (2015).
791 Synaptic Vesicle Exocytosis at the Dendritic Lobules of an Inhibitory Interneuron in the
792 Mammalian Retina. *Neuron*, *87*(3), 563–575. doi: 10.1016/j.neuron.2015.07.016

793 Berglund, K., Midorikawa, M., & Tachibana, M. (2002). Increase in the Pool Size of Releasable
794 Synaptic Vesicles by the Activation of Protein Kinase C in Goldfish Retinal Bipolar Cells. *The*
795 *Journal of Neuroscience*, *22*(12), 4776–4785. doi: 10.1523/jneurosci.22-12-04776.2002

796 Cao, Y., Posokhova, E., & Martemyanov, K. A. (2011). TRPM1 Forms Complexes with
797 Nyctalopin In Vivo and Accumulates in Postsynaptic Compartment of ON-Bipolar Neurons in
798 mGluR6-Dependent Manner. *The Journal of Neuroscience*, *31*(32), 11521–11526. doi:
799 10.1523/jneurosci.1682-11.2011

800 Cao, Y., Sarria, I., Fehlhaber, K. E., Kamasawa, N., Orlandi, C., James, K. N., … Martemyanov,
801 K. A. (2015). Mechanism for Selective Synaptic Wiring of Rod Photoreceptors into the
802 Retinal Circuitry and Its Role in Vision. *Neuron*, *87*(6), 1248–1260. doi:
803 10.1016/j.neuron.2015.09.002

804 Cao, Y., Wang, Y., Dunn, H. A., Orlandi, C., Shultz, N., Kamasawa, N., … Martemyanov, K. A.
805 (2020). Interplay between cell-adhesion molecules governs synaptic wiring of cone
806 photoreceptors. *Proceedings of the National Academy of Sciences*, *117*(38), 23914–23924.
807 doi: 10.1073/pnas.2009940117

808 Chávez, A. E., Grimes, W. N., & Diamond, J. S. (2010). Mechanisms Underlying Lateral
809 GABAergic Feedback onto Rod Bipolar Cells in Rat Retina. *The Journal of Neuroscience*,
810 *30*(6), 2330–2339. doi: 10.1523/jneurosci.5574-09.2010

811 Chávez, A. E., Singer, J. H., & Diamond, J. S. (2006). Fast neurotransmitter release triggered
812 by Ca influx through AMPA-type glutamate receptors. *Nature*, *443*(7112), 705–708. doi:
813 10.1038/nature05123

814 Chen, M., & von Gersdorff, H. (2019). How to Build a Fast and Highly Sensitive Sound Detector
815 That Remains Robust to Temperature Shifts. *The Journal of Neuroscience*, *39*(37), 7260–
816 7276. doi: 10.1523/jneurosci.2510-18.2019

817 Dong, C.-J., Agey, P., & Hare, W. A. (2004). Origins of the electroretinogram oscillatory
818 potentials in the rabbit retina. *Visual Neuroscience*, *21*(4), 533–543. doi:
819 10.1017/s0952523804214043

820 Dong, C.-J., & Hare, W. A. (2000). Contribution to the kinetics and amplitude of the
821 electroretinogram b-wave by third-order retinal neurons in the rabbit retina. *Vision Research*,
822 *40*(6), 579–590. doi: 10.1016/s0042-6989(99)00203-5

Dong, C.-J., & Hare, W. A. (2003). Temporal Modulation of Scotopic Visual Signals by A17 Amacrine Cells in Mammalian Retina In Vivo. *Journal of Neurophysiology*, *89*(4), 2159–2166. doi: 10.1152/jn.01008.2002

Doussau, F., & Augustine, G. J. (2000). The actin cytoskeleton and neurotransmitter release: An overview. *Biochimie*, *82*(4), 353–363. doi: 10.1016/s0300-9084(00)00217-0

Eggermann, E., Bucurenciu, I., Goswami, S. P., & Jonas, P. (2012). Nanodomain coupling between Ca2+ channels and sensors of exocytosis at fast mammalian synapses. *Nature Reviews Neuroscience*, *13*(1), 7–21. doi: 10.1038/nrn3125

Euler, T., & Masland, R. H. (2000). Light-Evoked Responses of Bipolar Cells in a Mammalian Retina. *Journal of Neurophysiology*, *83*(4), 1817–1829. doi: 10.1152/jn.2000.83.4.1817

Famiglietti, E. V., & Kolb, H. (1975). A bistratified amacrine cell and synaptic cirucitry in the inner plexiform layer of the retina. *Brain Research*, *84*(2), 293–300.

Fletcher, E. L., Koulen, P., & Wässle, H. (1998). GABAA and GABAC receptors on mammalian rod bipolar cells. *Journal of Comparative Neurology*, *396*(3), 351–365. doi: 10.1002/(sici)1096-9861(19980706)396:3<351::aid-cne6>3.0.co;2-1

Gillis, K. D. (2000). Admittance-based measurement of membrane capacitance using the EPC-9 patch-clamp amplifier. *Pflügers Archiv*, *439*(5), 655–664. doi: 10.1007/s004249900173

Grimes, W. N., Zhang, J., Graydon, C. W., Kachar, B., & Diamond, J. S. (2010). Retinal Parallel Processors: More than 100 Independent Microcircuits Operate within a Single Interneuron. *Neuron*, *65*(6), 873–885. doi: 10.1016/j.neuron.2010.02.028

Grimes, W. N., Zhang, J., Tian, H., Graydon, C. W., Hoon, M., Rieke, F., & Diamond, J. S. (2015). Complex inhibitory microcircuitry regulates retinal signaling near visual threshold. *Journal of Neurophysiology*, *114*(1), 341–353. doi: 10.1152/jn.00017.2015

Hartveit, E. (1996). Membrane currents evoked by ionotropic glutamate receptor agonists in rod bipolar cells in the rat retinal slice preparation. *Journal of Neurophysiology*, *76*(1), 401–422. doi: 10.1152/jn.1996.76.1.401

Hartveit, E. (1999). Reciprocal Synaptic Interactions Between Rod Bipolar Cells and Amacrine Cells in the Rat Retina. *Journal of Neurophysiology*, *81*(6), 2923–2936. doi: 10.1152/jn.1999.81.6.2923

Hasan, N., Pangeni, G., Cobb, C. A., Ray, T. A., Nettesheim, E. R., Ertel, K. J., … Gregg, R. G. (2019). Presynaptic Expression of LRIT3 Transsynaptically Organizes the Postsynaptic Glutamate Signaling Complex Containing TRPM1. *Cell Reports*, *27*(11), 3107-3116.e3. doi: 10.1016/j.celrep.2019.05.056

Hasan, N., Pangeni, G., Ray, T. A., Fransen, K. M., Noel, J., Borghuis, B. G., … Gregg, R. G. (2020). LRIT3 is required for Nyctalopin expression and normal ON and OFF pathway signaling in the retina. *ENeuro*, *7*(1), ENEURO.0002-20.2020. doi: 10.1523/eneuro.0002-20.2020

Hasan, N., Ray, T. A., & Gregg, R. G. (2016). CACNA1S expression in mouse retina: Novel isoforms and antibody cross-reactivity with GPR179. *Visual Neuroscience*, *33*, E009. doi: 10.1017/s0952523816000055

He, P., Jiang, S., Ma, M., Wang, Y., Li, R., Fang, F., … Zhang, Z. (2015). Trophoblast glycoprotein promotes pancreatic ductal adenocarcinoma cell metastasis through Wnt/planar cell polarity signaling. *Molecular Medicine Reports*, *12*(1), 503–509. doi: 10.3892/mmr.2015.3412

Jarsky, T., Tian, M., & Singer, J. H. (2010). Nanodomain Control of Exocytosis Is Responsible for the Signaling Capability of a Retinal Ribbon Synapse. *Journal of Neuroscience*, *30*(36), 11885–11895. doi: 10.1523/jneurosci.1415-10.2010

Job, C., & Lagnado, L. (1998). Calcium and Protein Kinase C Regulate the Actin Cytoskeleton in the Synaptic Terminal of Retinal Bipolar Cells. *The Journal of Cell Biology*, *143*(6), 1661–1672. doi: 10.1083/jcb.143.6.1661

Kagermeier-Schenk, B., Wehner, D., Özhan-Kizil, G., Yamamoto, H., Li, J., Kirchner, K., … Weidinger, G. (2011). Waif1/5T4 Inhibits Wnt/β-Catenin Signaling and Activates Noncanonical Wnt Pathways by Modifying LRP6 Subcellular Localization. *Developmental Cell*, *21*(6), 1129–1143. doi: 10.1016/j.devcel.2011.10.015

Kim, M.-H., & von Gersdorff, H. (2016). Postsynaptic Plasticity Triggered by Ca2+-Permeable AMPA Receptor Activation in Retinal Amacrine Cells. *Neuron*, *89*(3), 507–520. doi: 10.1016/j.neuron.2015.12.028

Klyachko, V. A., & Jackson, M. B. (2002). Capacitance steps and fusion pores of small and large-dense-core vesicles in nerve terminals. *Nature*, *418*(6893), 89–92. doi: 10.1038/nature00852

Kobe, B., & Deisenhofer, J. (1994). The leucine-rich repeat: a versatile binding motif. *Trends in Biochemical Sciences*, *19*(10), 415–421. doi: 10.1016/0968-0004(94)90090-6

Kobe, B., & Kajava, A. V. (2001). The leucine-rich repeat as a protein recognition motif. *Current Opinion in Structural Biology*, *11*(6), 725–732. doi: 10.1016/s0959-440x(01)00266-4

Koike, C., Numata, T., Ueda, H., Mori, Y., & Furukawa, T. (2010). TRPM1: A vertebrate TRP channel responsible for retinal ON bipolar function. *Cell Calcium*, *48*(2–3), 95–101. doi: 10.1016/j.ceca.2010.08.004

Koike, C., Obara, T., Uriu, Y., Numata, T., Sanuki, R., Miyata, K., … Furukawa, T. (2010). TRPM1 is a component of the retinal ON bipolar cell transduction channel in the mGluR6 cascade. *Proceedings of the National Academy of Sciences*, *107*(1), 332–337. doi: 10.1073/pnas.0912730107

Korol, S., Leuenberger, P. M., Englert, U., & Babel, J. (1975). In vivo effects of glycine on retinal ultrastructure and averaged electroretinogram. *Brain Research*, *97*(2), 235–251. doi: 10.1016/0006-8993(75)90447-3

Kushmerick, C., Renden, R., & von Gersdorff, H. (2006). Physiological Temperatures Reduce the Rate of Vesicle Pool Depletion and Short-Term Depression via an Acceleration of Vesicle Recruitment. *The Journal of Neuroscience*, *26*(5), 1366–1377. doi: 10.1523/jneurosci.3889-05.2006

Masu, M., Iwakabe, H., Tagawa, Y., Miyoshi, T., Yamashita, M., Fukuda, Y., … Nakanishi, S. (1995). Specific deficit of the ON response in visual transmission by targeted disruption of the mGluR6 gene. *Cell*, *80*(5), 757–765. doi: 10.1016/0092-8674(95)90354-2

McGuire, B., Stevens, J., & Sterling, P. (1984). Microcircuitry of bipolar cells in cat retina. *The Journal of Neuroscience*, *4*(12), 2920–2938. doi: 10.1523/jneurosci.04-12-02920.1984

Minami, N., Berglund, K., Sakaba, T., Kohmoto, H., & Tachibana, M. (1998). Potentiation of transmitter release by protein kinase C in goldfish retinal bipolar cells. *The Journal of Physiology*, *512*(1), 219–225. doi: 10.1111/j.1469-7793.1998.219bf.x

Morgans, C. W. (2000). Neurotransmitter release at ribbon synapses in the retina. *Immunology and Cell Biology*, *78*(4), 442–446. doi: 10.1046/j.1440-1711.2000.00923.x

Morgans, C. W., Brandstätter, J. H., Kellerman, J., Betz, H., & Wässle, H. (1996). A SNARE Complex Containing Syntaxin 3 Is Present in Ribbon Synapses of the Retina. *The Journal of Neuroscience*, *16*(21), 6713–6721. doi: 10.1523/jneurosci.16-21-06713.1996

Morgans, C. W., Zhang, J., Jeffrey, B. G., Nelson, S. M., Burke, N. S., Duvoisin, R. M., & Brown, R. L. (2009). TRPM1 is required for the depolarizing light response in retinal ON-bipolar cells. *Proceedings of the National Academy of Sciences*, *106*(45), 19174–19178. doi: 10.1073/pnas.0908711106

Moser, T., Grabner, C. P., & Schmitz, F. (2020). Sensory Processing at Ribbon Synapses in the Retina and the Cochlea. *Physiological Reviews*, *100*(1), 103–144. doi: 10.1152/physrev.00026.2018

Nakajima, Y., Iwakabe, H., Akazawa, C., Nawa, H., Shigemoto, R., Mizuno, N., & Nakanishi, S. (1993). Molecular characterization of a novel retinal metabotropic glutamate receptor mGluR6 with a high agonist selectivity for L-2-amino-4-phosphonobutyrate. *The Journal of Biological Chemistry*, *268*(16), 11868–11873.

Neher, E., & Marty, A. (1982). Discrete changes of cell membrane capacitance observed under conditions of enhanced secretion in bovine adrenal chromaffin cells. *Proceedings of the National Academy of Sciences*, *79*(21), 6712–6716. doi: 10.1073/pnas.79.21.6712

Neuillé, M., Cao, Y., Caplette, R., Guerrero-Given, D., Thomas, C., Kamasawa, N., … Zeitz, C. (2017). LRIT3 Differentially Affects Connectivity and Synaptic Transmission of Cones to ON- and OFF-Bipolar CellsLRIT3's Role in Cone to Bipolar Cell Transmission. *Investigative Ophthalmology & Visual Science*, *58*(3), 1768–1778. doi: 10.1167/iovs.16-20745

Neuillé, M., Morgans, C. W., Cao, Y., Orhan, E., Michiels, C., Sahel, J., … Zeitz, C. (2015). LRIT3 is essential to localize TRPM1 to the dendritic tips of depolarizing bipolar cells and may play a role in cone synapse formation. *European Journal of Neuroscience*, *42*(3), 1966–1975. doi: 10.1111/ejn.12959

Ogden, T. E. (1973). The oscillatory waves of the primate electroretinogram. *Vision Research*, *13*(6), 1059-IN4. doi: 10.1016/0042-6989(73)90144-2

Oltedal, L., & Hartveit, E. (2010). Transient release kinetics of rod bipolar cells revealed by capacitance measurement of exocytosis from axon terminals in rat retinal slices. *The Journal of Physiology*, *588*(9), 1469–1487. doi: 10.1113/jphysiol.2010.186916

Oltedal, L., Veruki, M. L., & Hartveit, E. (2009). Passive membrane properties and electrotonic signal processing in retinal rod bipolar cells. *The Journal of Physiology*, *587*(4), 829–849. doi: 10.1113/jphysiol.2008.165415

Palmer, M. J. (2006). Functional segregation of synaptic GABAA and GABAC receptors in goldfish bipolar cell terminals. *The Journal of Physiology*, *577*(1), 45–53. doi: 10.1113/jphysiol.2006.119560

Pearring, J. N., Bojang, P., Shen, Y., Koike, C., Furukawa, T., Nawy, S., & Gregg, R. G. (2011). A Role for Nyctalopin, a Small Leucine-Rich Repeat Protein, in Localizing the TRP Melastatin 1 Channel to Retinal Depolarizing Bipolar Cell Dendrites. *The Journal of Neuroscience*, *31*(27), 10060–10066. doi: 10.1523/jneurosci.1014-11.2011

Protti, D. A., & Llano, I. (1998). Calcium Currents and Calcium Signaling in Rod Bipolar Cells of Rat Retinal Slices. *Journal of Neuroscience*, *18*(10), 3715–3724. doi: 10.1523/jneurosci.18-10-03715.1998

Raviola, E., & Dacheux, R. F. (1987). Excitatory dyad synapse in rabbit retina. *Proceedings of the National Academy of Sciences*, *84*(20), 7324–7328. doi: 10.1073/pnas.84.20.7324

Robson, J. G., & Frishman, L. J. (2014). The rod-driven a-wave of the dark-adapted mammalian electroretinogram. *Progress in Retinal and Eye Research*, *39*, 1–22. doi: 10.1016/j.preteyeres.2013.12.003

Schindelin, J., Arganda-Carreras, I., Frise, E., Kaynig, V., Longair, M., Pietzsch, T., … Cardona, A. (2012). Fiji: an open-source platform for biological-image analysis. *Nature Methods*, *9*(7), 676–682. doi: 10.1038/nmeth.2019

Schulz, D. J., Baines, R. A., Hempel, C. M., Li, L., Liss, B., & Misonou, H. (2006). Cellular Excitability and the Regulation of Functional Neuronal Identity: From Gene Expression to Neuromodulation. *Journal of Neuroscience*, *26*(41), 10362–10367. doi: 10.1523/jneurosci.3194-06.2006

Shen, Y., Heimel, J. A., Kamermans, M., Peachey, N. S., Gregg, R. G., & Nawy, S. (2009). A Transient Receptor Potential-Like Channel Mediates Synaptic Transmission in Rod Bipolar Cells. *The Journal of Neuroscience*, *29*(19), 6088–6093. doi: 10.1523/jneurosci.0132-09.2009

Singer, J. H., & Diamond, J. S. (2003). Sustained Ca2+ Entry Elicits Transient Postsynaptic Currents at a Retinal Ribbon Synapse. *Journal of Neuroscience*, *23*(34), 10923–10933. doi: 10.1523/jneurosci.23-34-10923.2003

973 Sinha, R., Grimes, W. N., Wallin, J., Ebbinghaus, B. N., Luu, K., Cherry, T., … Hoon, M. (2021).
974 Transient expression of a GABA receptor subunit during early development is critical for
975 inhibitory synapse maturation and function. *Current Biology*, *31*(19), 4314-4326.e5. doi:
976 10.1016/j.cub.2021.07.059

977 Sinha, R., Siddiqui, T. J., Padmanabhan, N., Wallin, J., Zhang, C., Karimi, B., … Hoon, M.
978 (2020). LRRTM4: A Novel Regulator of Presynaptic Inhibition and Ribbon Synapse
979 Arrangements of Retinal Bipolar Cells. *Neuron*, *105*(6), 1007-1017.e5. doi:
980 10.1016/j.neuron.2019.12.028

981 Stockton, R. A., & Slaughter, M. M. (1989). B-wave of the electroretinogram. A reflection of ON
982 bipolar cell activity. *The Journal of General Physiology*, *93*(1), 101–122. doi:
983 10.1085/jgp.93.1.101

984 Tachibana, M. (1999). Regulation of transmitter release from retinal bipolar cells. *Progress in*
985 *Biophysics and Molecular Biology*, *72*(2), 109–133. doi: 10.1016/s0079-6107(99)00003-6

986 tom Dieck, S., & Brandstätter, J. H. (2006). Ribbon synapses of the retina. *Cell and Tissue*
987 *Research*, *326*(2), 339–346. doi: 10.1007/s00441-006-0234-0

988 Tsuboi, A. (2020). LRR-Containing Oncofetal Trophoblast Glycoprotein 5T4 Shapes Neural
989 Circuits in Olfactory and Visual Systems. *Frontiers in Molecular Neuroscience*, *13*, 581018.
990 doi: 10.3389/fnmol.2020.581018

991 Vaegan, & Millar, T. J. (1994). Effect of kainic acid and NMDA on the pattern electroretinogram,
992 the scotopic threshold response, the oscillatory potentials and the electroretinogram in the
993 urethane anaesthetized cat. *Vision Research*, *34*(9), 1111–1125. doi: 10.1016/0042-
994 6989(94)90294-1

995 Vardi, N., Duvoisin, R., Wu, G., & Sterling, P. (2000). Localization of mGluR6 to dendrites of ON
996 bipolar cells in primate retina. *Journal of Comparative Neurology*, *423*(3), 402–412. doi:
997 10.1002/1096-9861(20000731)423:3<402::aid-cne4>3.0.co;2-e

998 von Gersdorff, H., Vardi, E., Matthews, G., & Sterling, P. (1996). Evidence That Vesicles on the
999 Synaptic Ribbon of Retinal Bipolar Neurons Can Be Rapidly Released. *Neuron*, *16*(6), 1221–
1000 1227. doi: 10.1016/s0896-6273(00)80148-8

1001 Wachtmeister, L. (1998). Oscillatory potentials in the retina: what do they reveal. *Progress in*
1002 *Retinal and Eye Research*, *17*(4), 485–521. doi: 10.1016/s1350-9462(98)00006-8

1003 Wakeham, C. M., Ren, G., & Morgans, C. W. (2020). Expression and distribution of trophoblast
1004 glycoprotein in the mouse retina. *Journal of Comparative Neurology*, *528*(10), 1660–1671.
1005 doi: 10.1002/cne.24850

1006 Wakeham, C. M., Wilmarth, P. A., Cunliffe, J. M., Klimek, J. E., Ren, G., David, L. L., &
1007 Morgans, C. W. (2019). Identification of PKCα-dependent phosphoproteins in mouse retina.
1008 *Journal of Proteomics*, *206*, 103423. doi: 10.1016/j.jprot.2019.103423

1009 Xiong, W.-H., Pang, J.-J., Pennesi, M. E., Duvoisin, R. M., Wu, S. M., & Morgans, C. W. (2015).
1010 The Effect of PKCα on the Light Response of Rod Bipolar Cells in the Mouse Retina.
1011 *Investigative Ophthalmology & Visual Science*, *56*(8), 4961–4974. doi: 10.1167/iovs.15-
1012 16622

1013 Xu, Y., Dhingra, A., Fina, M. E., Koike, C., Furukawa, T., & Vardi, N. (2012). mGluR6 deletion
1014 renders the TRPM1 channel in retina inactive. *Journal of Neurophysiology*, *107*(3), 948–957.
1015 doi: 10.1152/jn.00933.2011

1016 Yoshihara, S.-I., Takahashi, H., Nishimura, N., Naritsuka, H., Shirao, T., Hirai, H., … Tsuboi, A.
1017 (2012). 5T4 Glycoprotein Regulates the Sensory Input-Dependent Development of a Specific
1018 Subtype of Newborn Interneurons in the Mouse Olfactory Bulb. *The Journal of Neuroscience*,
1019 *32*(6), 2217–2226. doi: 10.1523/jneurosci.5907-11.2012

1020 Zanazzi, G., & Matthews, G. (2009). The Molecular Architecture of Ribbon Presynaptic
1021 Terminals. *Molecular Neurobiology*, *39*(2), 130–148. doi: 10.1007/s12035-009-8058-z

1022 Zhao, Y., Malinauskas, T., Harlos, K., & Jones, E. Y. (2014). Structural Insights into the
1023 Inhibition of Wnt Signaling by Cancer Antigen 5T4/Wnt-Activated Inhibitory Factor 1.
1024 *Structure*, *22*(4), 612–620. doi: 10.1016/j.str.2014.01.009

1025 Zhou, Z.-Y., Wan, Q.-F., Thakur, P., & Heidelberger, R. (2006). Capacitance Measurements in
1026 the Mouse Rod Bipolar Cell Identify a Pool of Releasable Synaptic Vesicles. *Journal of*
1027 *Neurophysiology*, *96*(5), 2539–2548. doi: 10.1152/jn.00688.2006

1028